Nicolae Rodideal

BSc in Mechanical Engineering

Mechanical characterization and fatigue assessment of wire and arc additive manufactured HSLA steel parts

Thesis to obtain the MSc degree in Mechanical Engineering

Supervisor: Doctor Catarina Isabel Silva Vidal
Assistant Professor, Faculdade de Ciências e Tecnologia da Universidade Nova de Lisboa

Co-Supervisor: Doctor Carla Maria Moreira Machado
Assistant Professor, Faculdade de Ciências e Tecnologia da Universidade Nova de Lisboa

FACULDADE DE CIÊNCIAS E TECNOLOGIA
UNIVERSIDADE NOVA DE LISBOA

December 2020

Mechanical characterization and fatigue assessment of wire and arc additive manufactured HSLA steel parts

“Para ser grande, sê inteiro: nada
Teu exagera ou exclui.
Sê todo em cada coisa. Põe quanto és
No mínimo que fazes.
Assim em cada lago a lua toda
Brilha, porque alta vive.”
Ricardo Reis

Acknowledgments

First and foremost, I would like to acknowledge the support provided by my both supervisor and co-supervisor Professor Catarina Vidal and Professor Carla Machado, respectively. Their constant presence, feedback and guidance from the very beginning made this work not only possible but also enjoyable.

Secondly, I thank Valdemar Duarte, Tiago Rodrigues, Mr. Antonio Campos and Mr. Paulo Magalhães, for their support and advice during the experimental work. To Francisco Ferreira, for having the patience and availability to help me with the microscopic observations and to Francisco Fialho and Pedro Fonseca for their friendship and cooperation during the many hours spent both on samples manufacturing and material characterization.

I thank Professor Telmo Santos for his advice during this investigation, especially with the eddy currents and electrical conductivity testing.

My sincere gratitude to Eng. Rui Maltez for producing the specimens intended for fatigue and tensile testing.

I also thank Professor Rui Silva for his time, explanations and review of the microscopic observations.

In equal extent, I appreciate all the help provided by Professor Virgínia Infante, João Marques and Luís Gonçalves at Instituto Superior Técnico, especially for providing the necessary equipment to carry out the fatigue and tensile testing as well as the SEM analysis.

And because without friends one's life experience would not be the same, I thank Miguel Buinho, Sofia Colaço, Francisco Cascalho, Gonçalo Nobre, Maria Inês Silva, Yegor Borovkov, Sergiy Tsyshkovskiy, Mihail Vasilache and Francisco Antunes for their companionship, unwavering support, and the many good moments lived together during these past 5 years. May our friendship go on for years to come.

I also express my profound and sincere gratitude towards Loredana. She is not only a true inspiration for me but her love, patience and encouragement during the last three years forced me to lever up and kept me going through the best of times and the worst of

times. I hope to be able to retrieve such unconditional support throughout our journey together.

Finally, to my brother Anton, for his unavailing support and always being there for me. To my little sister Sofia for teaching me unconditional love and bringing out the best in me. And to my parents, whom I owe everything I am today. More than anyone, is them I dedicate this work to and whom I express my most deep gratitude. I’m compelled to say that their sacrifices during these 23 years, were not in vain.

Resumo

O fabrico aditivo é considerado como um novo pilar da indústria 4.0. Visa, sobretudo, aumentar a produtividade, diminuindo o material desperdiçado e introduzir vantagens que superam as técnicas de fabrico convencionais. *Wire and Arc Additive Manufacturing (WAAM)*, uma das várias tecnologias de fabrico aditivo, usa um arco elétrico como fonte de calor para adicionar material. Caracteriza-se pela sua versatilidade e liberdade de produzir componentes através de uma deposição camada a camada. Apesar das vantagens evidentes demonstradas, existe ainda um longo caminho a percorrer para implementar de forma integral este processo na indústria. Um dos principais desafios a enfrentar passa por estudar as propriedades mecânicas em função das geometrias, do material e dos parâmetros adotados.

No presente documento, o objetivo passou por estudar as propriedades mecânicas e a resistência à fadiga de componentes em aço HSLA produzidos por esta tecnologia. Para este efeito, foram fabricados dois conjuntos diferentes de peças, um com baixa entrega térmica e outro com elevada entrega térmica, em que a variável que mudou foi a velocidade de translação da tocha. Cada conjunto foi constituído por três paredes com dimensões de 180 x 100 mm.

Todo o estudo decorreu focado em três zonas distintas da parede – zona inferior, intermédia e superior. Procedeu-se à caracterização do material fabricado, nomeadamente, ondulação, microestrutura, condutividade elétrica e dureza e realizaram-se ensaios de tração uniaxial e de fadiga, com posterior observação das superfícies de fratura através do Microscópio Eletrónico de Varrimento.

Os ensaios de fadiga foram realizados para os componentes de baixa entrega térmica. Os ensaios decorreram à temperatura ambiente, à amplitude de tensão constante, razão de tensões R=0.1 e frequências entre 12 Hz e 15 Hz. É apresentada a curva S-N correspondente aos ensaios efetuados, juntamente com uma discussão dentro do contexto dos resultados obtidos das restantes técnicas de caracterização implementadas.

Palavras-chave

Fabrico Aditivo, WAAM, Soldadura, Aço HSLA, Propriedades Mecânicas, Fadiga

Abstract

Additive manufacturing is one of the main foundations of Industry 4.0. It aims, particularly, to increase productivity, reducing material waste due to machining and bring many advantages that overcome the conventional manufacturing processes. *Wire and Arc Additive Manufacturing (WAAM)* is an additive manufacturing process that employs an electric arc as heat source in order to melt and add material. It shows great versatility and freedom to fabricate parts using a layer-by-layer method of deposition. Despite the clear advantages presented, there still needs more progress in order to make it industrially feasible. One of the main challenges it faces is studying the mechanical properties bet on the desired geometry, type of material and the adopted parameters before employing these components in critical operational loading conditions.

This dissertation aimed to assess the mechanical properties and fatigue resistance of HSLA parts manufactured by this technology. In this way, two type of samples were produced – one of low heat-input and another of high heat-input, in which the changing variable was the travel speed. For each type, three thin walled parts were obtained, measuring 180 x 100 mm each.

After manufacturing all the required samples, three different regions were analysed – bottom, middle and top. Next, all parts were assiduously prepared in order to proceed with material characterization as well as testing, specifically, waviness, microstructure, electrical conductivity, microhardness, uniaxial tensile tests and lastly fatigue tests, with subsequent fracture surface observation through Scanning Electron Microscope (SEM).

Fatigue tests were performed at room temperature on low heat-input samples with constant stress amplitude, stress ratio R=0.1 and frequencies between 12 Hz and 15 Hz. The S-N curve of the experimental results is presented along with an explanation within the context of the other characterization techniques results.

Keywords

Additive Manufacturing, WAAM, Welding, HSLA steel, Mechanical properties, Fatigue

Table of Contents

List of Figures

List of Tables

Nomenclature

AM	Additive manufacturing
ASTM	American Society for Testing and Materials
BJ	Binder jetting
CAD	Computer aided design
CTWD	Contact tip to work distance
DC	Direct current
DED	Direct energy deposition
DT	Destructive testing
E	Young's modulus
ECT	Eddy currents testing
EDM	Electrical discharge machining
f	Frequency
GMAW	Gas metal arc welding
GTAW	Gas tungsten arc welding
HAZ	Heat affected zone
HSLA	High strength low alloy
HV	Vickers hardness
I	Current intensity
LMD	Laser metal deposition
MAG	Metal active gas
MIG	Metal inert gas
N	Number of cycles
N_f	Number of cycles to fracture
NDT	Non-destructive testing
PAW	Plasma arc welding
PBF	Powder bed fusion
R	Stress ratio
RP	Rapid prototyping
S	Nominal stress
SD	Standard deviation
SEM	Scanning electron microscopy
SLM	Selective laser melting

t	Time
U_r	Modulus of resilience
U_T	Modulus of toughness
UTS	Ultimate tensile strength
V	Voltage
VIC	Video image correlation
YTS	Yield tensile stress
WAAM	Wire and Arc Additive Manufacturing
WFS	Wire feed speed
ε	Engineering strain
ε_f	Strain at fracture
ε_y	Yield strain
σ	Engineering stress
$\Delta\sigma$	Stress range
σ_a	Alternating stress
σ_m	Mean stress
σ_{max}	Maximum engineering stress
σ_{min}	Minimum engineering stress
σ_y	Yield tensile stress

1 Introduction

1.1 Overview and Motivation

Nowadays, the industry is shifting towards a new concept of manufacturing where sustainability plays an important role [1]. The 4th Industrial Revolution, or Industry 4.0, combines the technological achievements from the past years with a vision of future intelligent and automated production systems, through advanced information technologies and the processing of extensive amounts of data [2].

Over the years, the increase in product customization, geometry complexity and short time demands forced the existing manufacturing systems to readapt in order to meet these requirements. Thus, Additive Manufacturing (AM) presents itself as a key technology since it can create sophisticated objects with advanced quality and attributes using a layer-by-layer material deposition.

Among the different AM processes, Wire and Arc Additive Manufacturing (WAAM) has become a promising alternative to conventional machining, competing with laser metal deposition (LMD) or selective laser melting (SLM). WAAM offers high deposition rates, high quality and the feasibility of using materials that are otherwise difficult to process through the above-mentioned laser alternatives, such as the NiTi Shape Alloys [3]. Nonetheless, there are still many ongoing studies on WAAM to see its further development, mainly on Non-Destructive Testing (NDT), certification of AM parts, post-processing operations and finally, improvement of fatigue lifetime, where there is still a lack of studies.

1.2 Objectives

This investigation has the objective of contributing to the WAAM technology ongoing development as far as fatigue resistance is concerned. In order to obtain feasible results, it is necessary to conduct a set of complementary characterization techniques. In sum, this thesis has the following aims:

- to characterize the parts produced by WAAM before and after post-processing;
- to investigate the influence of the process heat input on the mechanical strength of the material;
- to determine their mechanical properties through tensile testing;
- to assess the fatigue life of HSLA specimens produced by WAAM;
- to assess the effect of post-processing parameters on the fatigue lifetime of these specimens;
- to analyse the tensile and fatigue fracture surfaces in order to determine the failure mode.

1.3 Thesis Structure

This document is organized in the following way:

Chapter 1: A brief introduction is presented, as well as the motivation and the main objectives to accomplish in this investigation.

Chapter 2: The state of the art of WAAM technology and the current perspectives on mechanical properties regarding this technology are presented. Moreover, fatigue testing is introduced and its current applications on WAAM parts.

Chapter3: Describes the manufacturing process of the thin-walled parts, as well as the experiments that were conducted in order to proceed to material characterization.

Chapter 4: This is one of the most important chapters of this document, as it presents and discusses the essential results from the conducted experiments.

Chapter 5: The last chapter is dedicated to present the main conclusions derived from the present study together with the contributions made towards the progress of WAAM technology. And additionally, suggestions of future development are proposed.

2 Literature Review

2.1 Additive Manufacturing

Additive Manufacturing (AM) is a recent technique with several variants, which has become more and more important to many industries, such as automotive, aerospace, defence or biomedical, where a great magnitude has been achieved only in the last 10 years. AM technologies are based on Rapid Prototyping (RP), using the concept of slicing a Computer Aided Design (CAD) model and building it in a layer-by-layer mode using heat input (laser, electronic beam, electric arc, ultrasonic energy) and feedstock (metal powder, wire, thin metal sheet) [4].

Metals are highly used in engineering applications due to their favorable mechanical properties. Therefore, engineers have been aiming for solutions to integrate AM in industry in order to create metallic parts that are able to replace their conventionally produced counterparts. As a result, there are many advantages associated with this technology, mainly, the production of geometrical complex objects which in turn leads to less components for each assembly, the reduction of wasted material, less probability of human error, in-situ monitoring and an overall reduction of costs due to a shorter product development cycle [5].

As AM saw its emergence at an almost exponential level in the past years, there has been a difficulty to sort the existing processes in a viable category for educational and technical purposes. Given this, ASTM classifies AM technologies in seven categories, namely: Binder Jetting (BJ), Directed Energy Deposition (DED), Material Extrusion, Material Jetting, Powder Bed Fusion (PBF), Sheet Lamination and Vat Polymerization [6]. These categories are listed in Table 2.1, as well as a brief corresponding description.

Table 2.1 – AM categories and corresponding description according to ASTM [6].

Category	Definition
Binder Jetting	- An additive manufacturing process in which a liquid bonding agent is selectively deposited to join powder materials.
Directed Energy Deposition	- An additive manufacturing process in which focused thermal energy is used to fuse materials by melting as they are being deposited.
Material Extrusion	- An additive manufacturing process in which material is selectively dispensed through a nozzle or orifice.
Material Jetting	- An additive manufacturing process in which droplets of build material are selectively deposited.
Powder Bed Fusion	- An additive manufacturing process in which thermal energy selectively fuses regions of a powder bed.
Sheet Lamination	- An additive manufacturing process in which sheets of material are bonded to form an object.
Vat Photopolymerization	- An additive manufacturing process in which liquid photopolymer in a vat is selectively cured by light-activated polymerization.

However, the most common AM processes in today's industry fall into two categories, PBF and DED, which depend upon the employed method of delivering the feedstock material. While PBF based processes are described as high precision methods in which parts are produced by selectively melting regions of a powder bed using thermal energy [7], DED processes are characterized by injecting material feedstock into the melt pool. Figure 2.1 displays the most common processes that are inherent to the two categories mentioned above.

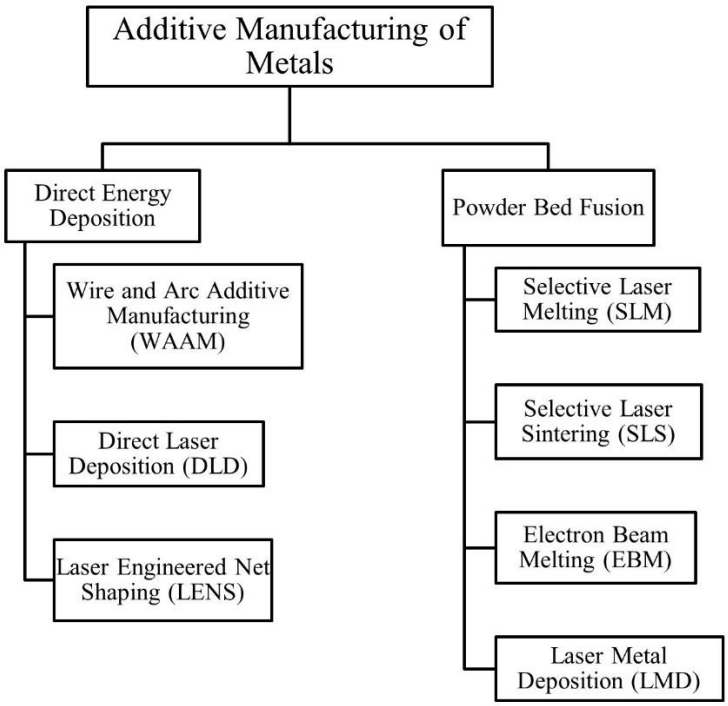

Figure 2.1 – Common technologies of metal AM.

AM is revolutionizing the manufacturing paradigm as new studies are being developed, driving this technology to a status where it can reduce the human interaction and produce complex near-net shape components, leading to the idea of what is known as smart factories, which play an important role in the industry 4.0. Today, most AM processes focuses on powder-bed systems or/and electron beams as heat sources owing the high precision of dimensional tolerances, high quality, and process automation. Yet, these lack satisfactory deposition rates, which increases lead times, are size limited and have defects, namely porosities, that are prone to occur considering the feedstock used, which can hinder product lifetime once exposed to dynamic solicitation conditions [8]. Consequently, new means of manufacturing are on the rise, being WAAM one of them. Using an electric arc as heat source, this technique answers to situations where high deposition rates, low costs and medium to large size objects are requested.

2.2 Wire and Arc Additive Manufacturing

Whereas PBF technologies make use of laser or electron beams as heat sources, WAAM is a DED process that relies on an electric arc in order to inject feedstock material

into the weld pool, which erases the need of a vacuum environment and additionally presents a higher energy efficiency when using reflective metal alloys as feedstock material. In addition, as stated above, this process claims high deposition rates, good structural integration, low equipment cost, high material utilization and often better materials properties than their wrought counterparts [9,10]. This makes WAAM a suitable candidate to replace current technologies that draw on manufacturing methods as solid billets or large forgings [11–13], and meet the demanding requirements from aerospace, automotive and rapid tooling industry [14].

WAAM is traced back to the 1920s [15], however, it has only seen major developments in the last ten years, becoming a promising fabrication process that enables the use of materials as titanium, nickel alloys, aluminium, magnesium and steel. This technology relies on welding processes that already exist and are largely developed; thus, there are three main welding processes currently used: gas metal arc welding (GMAW), gas tungsten arc welding (GTAW), and plasma arc welding (PAW). Out of these three, PAW and GTAW demonstrated to be more reliable processes due to their arc stability, fewer spattering, heating, distortions and porosity. However, because of the wire being fed externally, and not coaxially as in GMAW, it leads to process variations once the path direction is changed. As described in Table 2.2, these variants require an axis of rotation for both torch and wire, which limits the process applicability.

This leaves GMAW as the most used technique. This process has a continuously fed wire electrode through a nozzle and is often referred as MAG, which stands for metal active gas, or MIG when an inert gas is used. Opposite to GTAW and PAW, GMAW does not require a rotary axis due to its wire being fed coaxially as the arc is formed, Figure 2.2. This accounts for, consistent metal deposition that improves grain morphology, higher overall productivity, allowing the production of large-scale parts in short time spans. The welding arc is formed between the consumable wire electrode and the workpiece metal usually under DC current.

According to the set of parameters and the energy source, there are four primary types of metal transfer, called globular, short circuit, spray and pulsed spray. Metal transfer mode will affect the weld shape, heat input, spatter and the ability to weld in different positions [16]. Thereby, special attention must be given to each situation in order to obtain the desired results.

Table 2.2 – WAAM techniques comparisons [18, 19].

Technique	Variant	Features
GTAW-based	GTAW	• Tungsten electrode (non-consumable); • External wire feed; • Wire and torch rotation system needed; • Ideal for highly reactive materials (Aluminium, Titanium, etc.); • Deposition rates 1-1.5 kg/h;
GMAW-based	GMAW	• Consumable wire electrode; • Arc stability problems, spattering; • Higher deposition rates, up to 9 kg/h;
	Cold Metal Transfer (CMT)	• Reduced heat input; • More stable than GMAW, no spatter; • Incorporated control system controls the transfers mode; • 2-3 kg/h deposition rates; • High dimensional tolerances;
	Tandem GMAW	• Two wires fed into the melt pool; • High deposition rates 6-9 kg/h; • Requires high amount of energy to maintain the arc;
PAW-based	PAW	• Separate wire feed; • Non-consumable electrode; • High-energy density process, which increases arc stability; • High metal deposition; • Wire and torch rotation system needed;

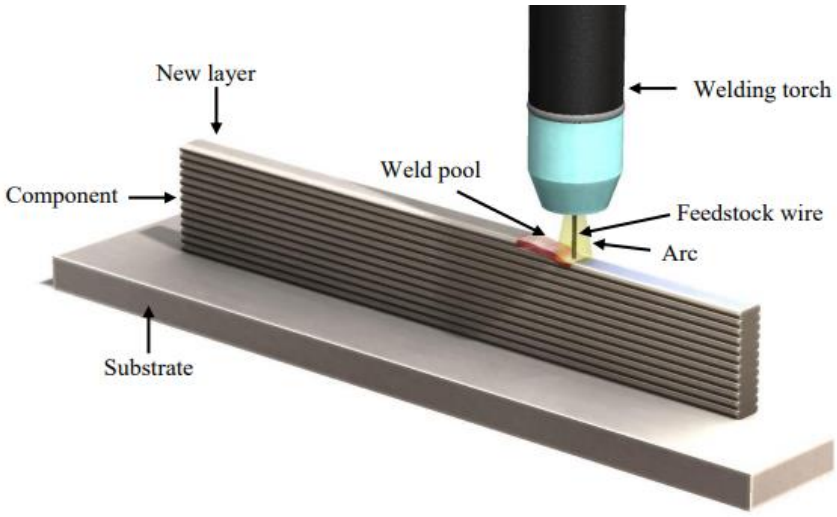

Figure 2.2 – Schematic representation of WAAM based on GMAW variant [17].

Up to this point many solutions have come forward to give answers to many problems inherent to this technology. However, there are still many barriers imposed, as for example the lack of accuracy of the as-built parts caused by the "stair-stepping" effect [14] or the lack of reproducibility associated with WAAM, which causes problems regarding standardisation and certification. Therefore, NDT (Non-Destructive Testing) and on-line monitoring must be developed further still, to adequately adjust to this technology.

Moreover, WAAM continues to undergo constant development. For instance, Lopes *et al.* [20] studied the feasibility of milling HSLA parts and showed the cutting tool wear overtime, since post-processing constitutes a major problem.

Consequently, and equally important, there is a lack of knowledge on how post-processing influences the fatigue lifetime of these components. This thesis aims to contribute to answer to this problem.

2.2.1 Process Parameters

In welding technology, parameters are controlled to obtain viable results. What makes welding such an interesting and fascinating field of study is that overall, there are no perfect solutions. All in one, there is a compromise between different parameters that sets one near the desired solution. Nonetheless, every parameter brings changes and thus, directly affects the welding bead and so, the final product.

WAAM seeks its functional principle in the conventional welding technology of the aforementioned GMAW, GTAW or PAW. Being GMAW mostly used, the main parameters of this variant are listed in Table 2.3.

Table 2.3 – Main parameters of GMAW in WAAM.

Parameter
Current Intensity (I)
Voltage (V)
Welding Shielding Gas
Travel Speed
Wire Feed Speed (WFS)
Gas Flow Rate
Electrode Extension

Current intensity dictates the weld penetration as well as the deposition rate and is almost linear to the WFS, whereas voltage determines the arc length and the amount of heat input. An important remark regarding these parameters is “the self-regulation” concept, which is inherent to this process. With self-regulation, the arc length is constantly adjusted by the power supply.

Welding shielding gas and gas flow rate are one of the most influent parameters, affecting the arc stability, bead geometry, transfer mode and weld aspect. Travel speed will influence the bead geometry and penetration. And last, electrode extension will affect both bead geometry, penetration and deposit rate. However, another important parameter, wherein electrode extension is included, is the contact tip to work distance (CTWD). Beside expressing the influence of the electrode extension, it gives information of the distance from the end of the contact tip to the work piece.

Since, each parameter has an impact on the weld quality, geometry and mechanical properties, they ought to be adjusted according to the substrate used, torch angle, type of electrode, its diameter and the required weld characteristics.

2.3 Mechanical Behaviour of Materials

Understanding material behaviour has always been at the core of our society since the early times. However, only recently in history an enormous progress has been made starting with the minds of Hooke, Mohr and Poisson, giving way to a better insight into the mechanical properties of materials, with special attention to metals. Given that materials are subjected to different types of loads when in service, it is of the utmost importance to know the characteristics of each material, for, when selecting and designing each component, the resulting deformation cannot be excessive and thus not lead to failure. Nowadays, designers rely on this field of study to guarantee not only acceptable levels of quality and performance, but also safety and durability, thus avoiding unwanted deformation and fracture [21–23].

2.3.1 Mechanical Testing

A fundamental step in engineering design is the selection of suitable materials that will integrate the final product. Materials testing ensures that the chosen materials fill in the requirements for specific loading cases and criteria, and further allows to make a qualitative and quantitative comparison among materials. In addition, through testing it is possible to determine materials properties, such as: fracture toughness, ultimate tensile stress (UTS), yield tensile stress (YTS), stiffness, hardness and elongation.

There are different types of testing techniques and these can be grouped in two categories – Destructive Testing (DT) and Non-Destructive Testing (NDT). NDT comprises a set of evaluation techniques used to detect defects, discontinuities and other material characteristics without causing damage to the test specimen. A few examples of NDT techniques are dye penetrant testing, eddy currents, ultrasonic testing, and visual inspection.

DT, on the other hand, includes testing techniques where mechanical properties and material behaviour are studied by carrying out experimental procedures that result in the test specimen's failure. In other words, these type of tests changes or destroys the part, making it no longer functional. Examples of DT are corrosion testing, uniaxial tensile testing, bend testing, impact testing, fatigue testing and fatigue crack growth rate testing.

One recurrent and highly used test method is uniaxial tensile testing. A test specimen is submitted to an increasing axial load until it fractures, allowing to determine material properties such as the Young's modulus, yield and tensile strengths and elongation to fracture. In today's industry it is also employed as acceptance tests and quality control following material specification. Moreover, it is recommended to follow specific standards that dictates the adequate procedure as well as specimens dimensions [24].

In this study, uniaxial tensile tests and fatigue tests will be used to characterize WAAM specimens. Fatigue is thus the topic discussed in the next section.

2.4 Fatigue

According to ASTM International, Fatigue is – "the process of progressive localized permanent structural change occurring in a material subjected to conditions which produce fluctuating stresses and strains at some point or points and which may culminate in cracks or complete fracture after a sufficient number of fluctuations" [25].

In early 19th century, August Wohler recognized that sometimes a single load applied to a structure did not induce any damage, however, if the same load was applied repeatedly it led to material failure [26]. Throughout the 20th century the attention on this phenomenon increased, essentially because of disasters that apparently were hard to explain at first sight. With the increase on the number of studies on this matter came up a deeper comprehension, which led to modifications in many industries as to the way structures were built and assembled. A fair example of this is the replacement of rectangular windows in aircrafts by round ones, given the stress concentration that these were subjected due to their geometry.

Thus, when in service, parts and structures are submitted to static and dynamic loads. However, dynamic loads are the primarily cause of failure of most of the components in industry. Fatigue is the term used to address this situation when a material is under constant dynamic solicitations, also described as a progressively weakening phenomena which leads the material to fracture or cease its normal functioning, and the maximum load required for this to occur is much less than the static breaking load. This phenomenon depends on the geometry and size, environment, manufacturing and surface conditions and loading type.

Once a component is subjected to repeated cycles, specific sections with surface discontinuity or geometry change, will be prone to accumulate more stress than the remaining parts. Over time, these highly stressed regions will suffer changes in microstructure that will finally lead to fracture. Figure 2.3 describes the four generic phases that characterizes the fatigue phenomenon. A dangerous fact about fatigue failures is that these do not seem to present any indication of plastic deformation prior to fracture in the cracking zone [27]. Thus, the prediction of crack propagation is one of the most studied aspects of fatigue.

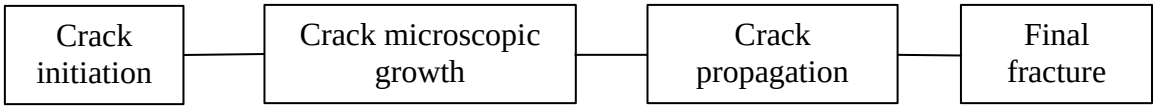

Figure 2.3 – Four phases of fatigue phenomenon (adapted from [22]).

The first two phases are characterized by crack nucleation and accumulated displacements at a microscopical level due to surface roughness or voids. Finally, the junction of instable discontinuities occurs in the last two phases, often seen at naked eye, leading to fracture in the last cycle of the fatigue life [22, 26, 28].

According to the number of cycles under which a part is subjected, there are two types of fatigue regimes. Low-cycle fatigue (LCF), on one hand, accounts for situations where fracture develops under a low number of cycles, usually below 10^4-10^5, and additionally, loading are often higher than the yield stress which leads to the predominance of plastic deformation Despite the low number of cycles, this condition may translate into low frequency loads and longer product lifetime. On the other hand, high-cycle fatigue (HCF), as the name suggests, is referred to situations when cycles overcome 10^4-10^5, and is most often studied due to applied stresses below the yield stress, which gains interest particularly in regions with stress concentration [22, 26]. Fatigue cycles can further be separated either into variable amplitude loading, Figure 2.4, or constant amplitude loading, Figure 2.5. Constant amplitude cycles with constant mean loads are predominant in rotary applications like gears systems and shafts. Whereas variable amplitude cycles are encountered in numerous situations, such as a plane wing or a bridge under wind conditions, for example.

Regarding to WAAM, the main concerns regarding fatigue failure are related to surface finishing, building strategy, the presence of waviness, porosity defects, lack of fusion and micro-cracks [29]. It is also proved that there are methods such as the ones carried out by P.A. Colegrove *et al.* [30] on Ti-6Al-4V material, where inter-layer cold rolling is applied and translated into fatigue strength twice that was required by the standards. Moreover, in defect-free parts and under static load conditions, mechanical strength is larger than in parts manufactured by conventional technologies, as long as using the correct parameters [13]. Nonetheless, given the freedom of design allowed by AM, it is recommended to avoid the manufacturing of sharp corners or other compromising geometries sections that are susceptible to accumulate stress, thus reducing the risk of failure.

2.4.1 Fatigue Testing

There are several types of tests carried under controlled conditions that allows the study of fatigue behaviour on materials, welded joints, structures, as well as the influence of the environment, the surface finishing, and the verification of fatigue prediction models. Crack growth analysis is usually performed under constant amplitude load conditions, where analytical results are then compared to empirical data. However, when in service, structures withstand variable amplitudes and sometimes even of random nature. This turns to be a difficulty when trying to accurately predict crack propagation.

As stated, variable cycles are very often in practical applications. Components may suffer from blocks loading cycle, Figure 2.4a, or random cycles, Figure 2.4b.

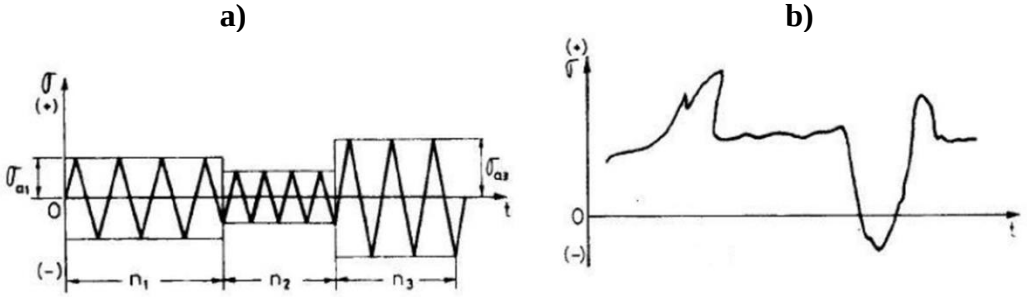

Figure 2.4 – Blocks cycle (a) and random or irregular cycle (b) [22].

The fatigue life of a component is described as the number of cycles, N_f, it can endure until it reaches the final fracture. Thus, N_f is the sum of the number of cycles required for the crack nucleation N_i and the number of cycles that leads to crack propagation N_p (2.1). The stress range experienced by a component under constant amplitude loading scenarios is given by the difference between the maximum and the minimum stress (2.2). The average of minimum and maximum values gives the mean stress σ_m (2.3a) and half the stress range gives the alternating stress σ_a (2.3b). Additionally, stress ratio is represented by R (2.4).

$$N_f = N_i + N_p \tag{2.1}$$

$$\Delta\sigma = \sigma_{max} - \sigma_{min} \tag{2.2}$$

$$\sigma_m = \frac{\sigma_{max} + \sigma_{min}}{2} \tag{2.3a}$$

$$\sigma_a = \frac{\sigma_{max} - \sigma_{min}}{2} \tag{2.3b}$$

$$R = \frac{\sigma_{min}}{\sigma_{max}} \tag{2.4}$$

Generally, for constant amplitude fatigue cycles the applied conditions are described as $\sigma_m \pm \sigma_a$, where the positive sign denotes tensile stress, and the negative sign denotes compressive stress. According to the mean stress value, Table 2.4 describes three different types of cycles for constant amplitude loading.

Table 2.4 – Type of cycles for constant amplitude fatigue.

Cycle	Description
Alternating cycle	When $\sigma_m = 0$, the maximum and minimum stresses are symmetrical and the cycle is generally described by a linear, sinusoidal, triangular or trapezoidal wave with frequency f denoting the ratio between the number of cycles N and the time t, (2.5). The Sinusoidal wave, Figure 2.5a, is very often used in real cases, and is described by equation (2.6).

Fluctuating cycle	Situation where $\sigma_m \neq 0$ and the cycle fluctuates between compressive stresses, tensile stresses or tensile and compressive stresses, Figure 2.5b.
Pulsating cycle	When $\sigma_m = \sigma_a$, the minimum stress is zero, Figure 2.5c.

$$f = \frac{N}{t} \tag{2.5}$$

$$\sigma - \sigma_m = \sigma_{max} sin\,(2\pi t f) \tag{2.6}$$

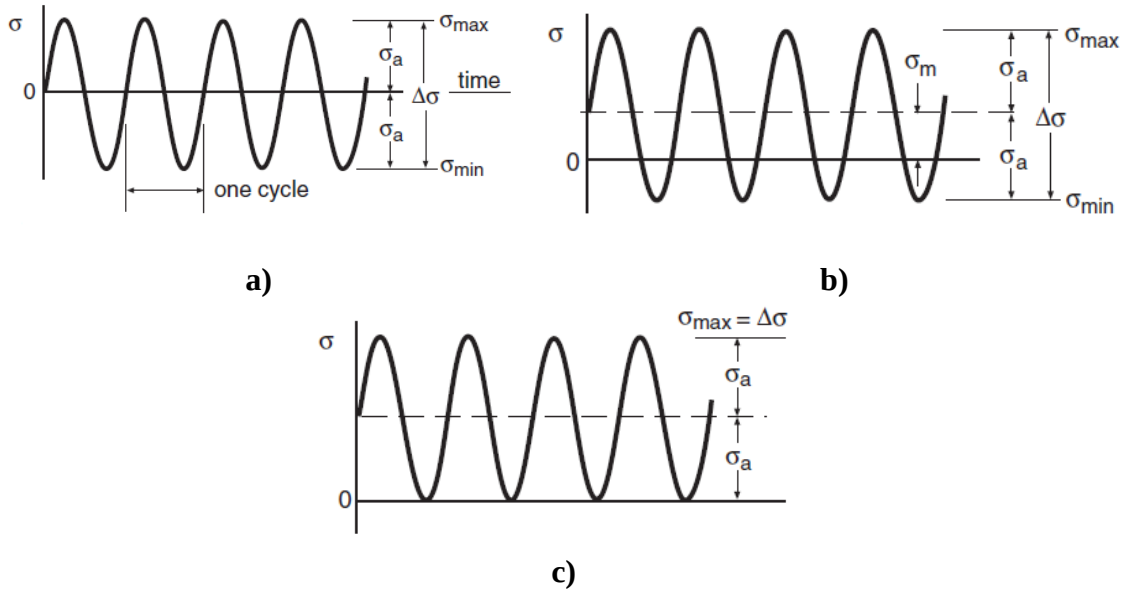

Figure 2.5 – Alternating cycle (a), Fluctuating cycle (b), Pulsating cycle (c).

There are different types of specimens that can be tested. These can be notched, as seen in Figure 2.6a), unnotched, Figure 2.6b), welded joints, riveted joints, etc. However, there are no fully unnotched specimens, since they all should present an area where there is a slightly higher stress concentration, represented by K_t, and additionally, it is of interest in engineering to study these specimens from a notch sensitivity point of view.

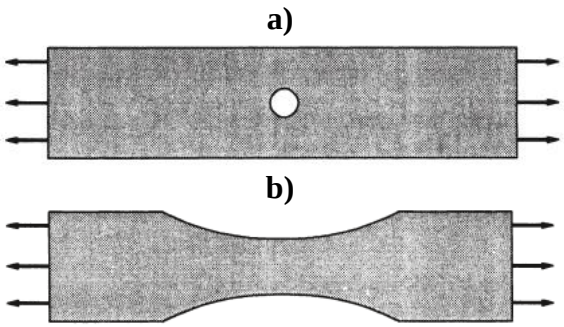

Figure 2.6 – a) Notched and b) (Quasi) unnotched specimen [26].

In addition, there are different types of fatigue tests that can be carried out to assess the fatigue behaviour of materials:

- Uniaxial testing
    - Rotating and flat bending (alternating, fluctuating or pulsating);
    - Alternating torsion;
    - Tension/compression (alternating, fluctuating or pulsating).

- Multiaxial testing
    - Alternating bending or tension;
    - Tension or compression;
    - Alternating torsion with static tension.

For this particular study on WAAM HSLA material, specimens will be produced according to ASTM International standards [31]. Data provided by fatigue testing is plotted on a S-N curve, i.e. stress range vs number of cycles to failure, on a bi-logarithmic scale since data can vary from thousands to millions of cycles. This is true when considering HCF tests. In the otherwise presence of LCF, S-N curves are seldom investigated given that strain is predominantly plastic. Tests, then, are carried out under strain-controlled conditions in this situation. The relation between stress and the number of cycles is given by equation (2.7). Where constants *m* and *C* depend on the material and test conditions.

$$\sigma^m \cdot N_f = C \tag{2.7}$$

Another way to represent the previous equation is through logarithmic notation, which is represented in equation (2.8):

$$log(\sigma) = A + B \cdot log\ (N_f) \tag{2.8}$$

A and B are constants that can be determined by linear regression. *A*, *B*, *m* and *C* are related in the following way:

$$A = \frac{1}{m}\log(C)\,; \qquad B = -\frac{1}{m} \tag{2.9}$$

2.5 Mechanical properties of WAAM components

As WAAM progressively sees its development in the manufacturing industry, more studies have been conducted regarding process conditions and how they influence the mechanical properties, thermal history and residual stresses of different materials processed by this technology. Suryakumar *et al.* [32] studied the correlation between thermal cycles and hardness along the building direction on a carbon steel ER70S-6 using a GMAW-based Hybrid layered manufacturing (HLA) process. Concluding that the number of layers influence the hardness of the product. The lower the number of layers, the more thermal cycles the part undergoes. Consequently, as observed in Figure 2.7, the top layers experience increased hardness. In the same study, results on mechanical properties showed that, although UTS varied as height increased, it was higher than that of conventional manufacturing processes like CNC.

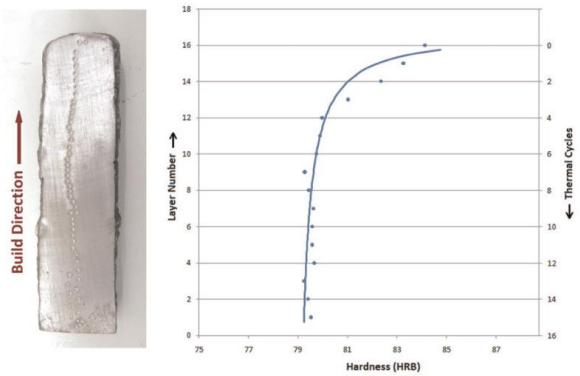

Figure 2.7 – Hardness evolution along the building direction [32].

Haden *et al.* [10] investigated mechanical properties on two steels, stainless steel 304 and mild steel ER70S comparing with their wrought parts. Wear rate was observed, and the highest value was detected at a printing point monotonically decreasing along the

welding direction for both specimens. Whereas, regarding porosity, there was no preferential direction according to their distribution. For stainless steel, YTS values exceeded those of the wrought part and varied both in the welding direction and height. UTS results, on the other hand, are similar to the wrought part, suggesting that thermal history has a greater impact in YTS than UTS. As for the mild steel, both YTS and UTS are similar to the wrought parts. The authors suggest that by careful toolpath planning and design, localized material properties can be controlled.

Additionally, further variants have been developed to mitigate common issues present in WAAM. Extensive distortions are one of the bigger concerns in wire-based AM processes, as well as large grain growth obtained because of great heat input and slow cooling rates. This is true especially in large-scale components, affecting the tolerances and inducing premature failure [33]. Inter-layer cold rolling, studied and developed by P.A Colegrove *et al.* at Cranfield [30], Figure 2.8, was proved to be a method able to solve not only porosity defects, which is also often-encountered in this technology, especially in aluminium alloys, but also reduce residual stresses, distortion issues and waviness. Equally, another method that efficiently reduces residual stresses is the pre-heating of the substrate. Alberti *el al.* [34], studied the material behaviour on a substrate with and without pre-heating, concluding that the latter results in a homogeneous temperature distribution, smaller temperature gradients, reduced thermal stresses and improved wettability and consequently improved mechanical properties.

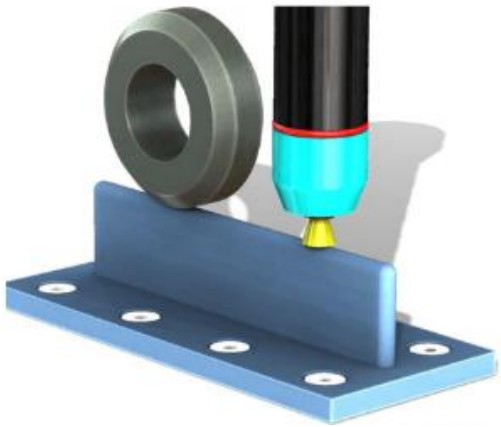

Figure 2.8 – In-situ monitoring of inter-layer rolling [30].

The maximum temperature achieved in each layer has a direct influence in the subsequent layer. In other words, the first layer melts and solidifies onto the substrate, once the second layer is deposited, it will introduce more heat, partially melting the

previous layer and itself. Moreover, there are a series of heating zones being created with each added layer as seen in multipass welding, Figure 2.9. This has implications in grain distribution and overall mechanical properties [13, 35]. Thus, another solution is to apply an in-process inter-layer cooling that eliminates the differences in heat dissipation between the upper and lower layer. This solution leads to improved production times, surface quality, dimensional tolerances, and a refined microstructure.

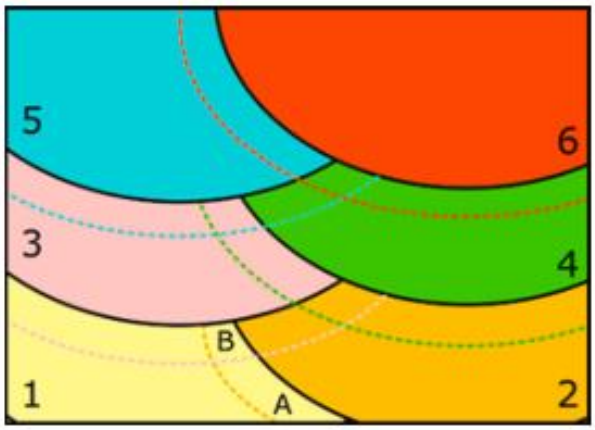

Figure 2.9 – Schematic representation of a multipass weld.

Regarding HSLA steels, these are structural materials designed to obtain increased mechanical properties by introducing elements to its microstructure, as niobium, titanium, vanadium, or aluminium. These steels were initially developed to replace low-carbon steels primarily due to their strength-to-weight ratio. Additionally, they experience a wide field of application, primarily due to their high strength, ductility, low temperature fracture toughness, higher weldability and reduced heat affected zone (HAZ) when compared with other high strength steels [36–38] . Hence, as far as WAAM is concerned, HSLA steels can bring several benefits, primarily because of their characteristics.

Research regarding thermal cycles was carried out by Rodrigues *et al.* [39] on HSLA thin-walled parts, using high-heat input and low-heat input specimens. It was observed that microhardness depends on the heat input, being higher and more uniform for low heat levels, while surface waviness decreased when used high-heat input. As for uniaxial tensile strength both specimens presented similar results, with high UTS and ductility.

Further literature review suggests that most of the work done to date focuses primarily on material microstructure, tension/compressive testing. Moreover, very little published

data exists regarding fracture properties, as toughness, fatigue or crack propagation [8, 9, 33]. As to HSLA steels, there is still a lack of research related to WAAM.

2.5.1 Fatigue of WAAM components

As already mentioned, fatigue behaviour of structures and parts is of major concern in industry. With special attention to WAAM technology, research has to be developed in order to evaluate how components behave under different environments [33]. So far, a number of studies were carried out regarding the fatigue relation with porosity defects and crack initiation [29, 40–46].

Gordon *et al.*, [42], investigated the crack growth using 304L austenitic stainless steel for specimens parallel and perpendicular to the building direction. Results were correlated to microstructure, residual stresses, and texture. It was observed that the building direction has influence on the fatigue behaviour, since vertical specimens showed better fatigue resistance, as can be seen in Figure 2.10. The differences between horizontal and vertical results were attributed to long columnar grains and strong texture in the build direction. Subsequently, compressive residual stress showed to positively affect crack growth when compared to stress relieved specimens [29]. Altogether, comparing with wrought 304L parts, the as-built specimens showed similar/increased results regarding fatigue performance.

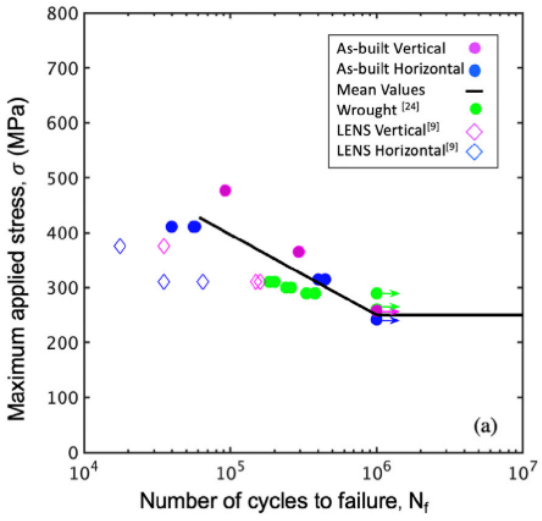

Figure 2.10 – S-N Curve for wrought and printed components.

Zhang *et al.* investigated crack growth rate and fracture toughness on Ti-6Al-4V WAAM processed parts [41]. Focusing on microstructure and residual stresses, the study

concluded that crack growth rate is smaller when compared to wrought parts and has a tortuous path. This occurs mainly because of the lamellar structure present in WAAM, whereas the wrought alloy has an equiaxed grain distribution producing a straight and smooth crack. The effect of residual stresses depends on the crack location and direction. As for porosity, Biswal *et al.* [43] carried out a study where two types of specimens of Ti-6Al-4V where compared. One group without porosity and another with designed porosity. It was observed that although static strength remained similar, specimens with porosity had a 60% elongation reduction and a 33% lower fatigue strength that the control group.

A recent investigation of Wachter *et al.* [47] aimed to determine the influence of inter layer temperature on material properties. Monotonic and fatigue testing was performed, as well as residual stresses were measured, on a medium strength steel material designed to weld low-alloyed high strength structural steels. Similar to the investigation performed in the present document, specimens from different regions were extracted and tested. It was observed that residual stresses tend to be higher and positive in the top region and more of compression in middle and top region, as depicted in Figure 2.11. Tensile strength results do not present significant variation, except for YTS, which was higher on the lower interlayer temperature samples. Regarding fatigue results, no pronounced trend was recognized, although, it was noted that the heat treatment led to compression-dominated residual stresses at the surface, which delayed fatigue failure that is known to be initiated in this region.

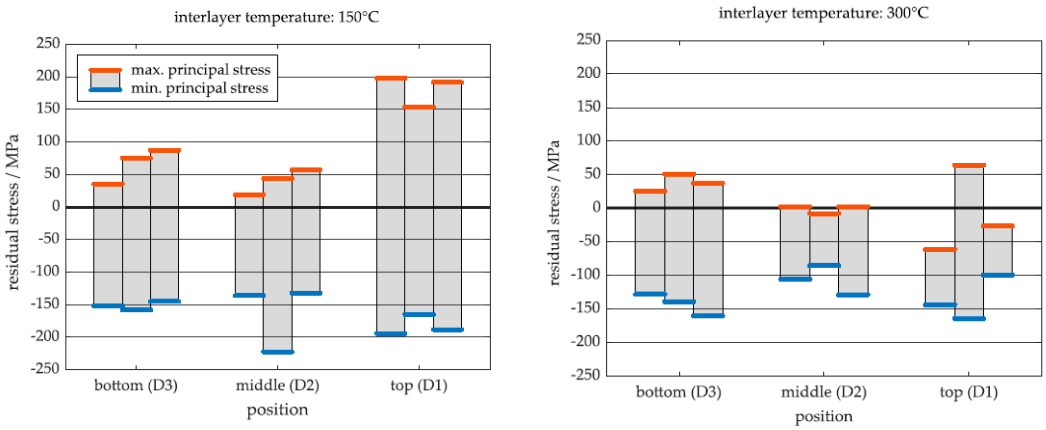

Figure 2.11 – Residual stresses along height on WAAM material.

As for HSLA steels, studies carried out by Bandgar *et al.* [40] or Ron *et al.* [48] can be found. However, these focus on a microstructural level, with a disregard for process

parameters or post-processing influence. Given the rough finishing of WAAM components, these have to be machined afterwards, thereby, great interest resides on the effect of post-processing and its parameters.

2.6 Chapter resume

It is clear that additive manufacturing with an electric arc has been intensively investigated by different universities and innovative hubs throughout the world. All aim to give this technology the necessary means to be implemented as another manufacturing process in the industry. From the literature review, it could be verified that, although it has many advantages, more investigation is necessary in order to this process be able to compete with other manufacturing technologies. Mechanical properties need to be studied as a function of geometry, consumables, or productivity.

The following chapters will intend to add more valuable information to this technology as it will portray the investigation that was performed, along with the main results that were obtained.

3 Experimental Procedure

3.1 Material specification and samples manufacture

There is great interest in understanding the influence of heat input on the mechanical properties of materials produced by WAAM. The interest rises from a productivity standpoint, as higher energy input will lead to shorter manufacturing times and lower costs. In this way, this research started off by manufacturing two types of thin-walled parts, one corresponding to a high heat-input and another to a low heat-input. The experimental apparatus consisted of a custom-built welding torch mounted on a three-axis positioning system. A *KEMPY* welding machine, with a power source Pro MIG 3200, wire feeder and control unit Pro MIG 501. For this purpose, inverse polarity (DCEP/DC+) was used.

The wire electrode employed was a commercial HSLA steel, AWS A5.28 ER110S-G, of 1 mm-diameter. This material can be used on a large set of applications, such as welding pressure vessels, ship repairing, tools and dies industries and in hoisting machinery. According to the manufacturer, the welding bead expresses a high tensile strength, fracture, and impact toughness. The chemical composition and mechanical proprieties are described in Table 3.1 and Table 3.2, respectively.

Table 3.1 – Chemical composition of the ER110S-G wire electrode [wt. %] [49].

C	Mn	Si	Ni	Cr	Mo	Fe
0.10	1.70	0.70	2.0	0.30	0.50	Balance

Table 3.2 – Mechanical properties of the ER110S-G wire electrode [49].

Yield Strength [MPa]	Tensile Strength [MPa]	Elongation [%]	Impact ISO-V [J]
880-920	940-980	20-16%	95-65

The experimental approach was identical to that used in [39]. Differing only on the deposition strategy. A zig-zag deposition was performed, as in [20], aiming to achieve uniform heat distribution along the wall and a levelled structure in terms of height, as seen in Figure 3.1. The samples' dimensions were set to 180 mm in length and 100 mm in height. A CTWD of 7 mm was set, which was held constant with each additional layer. To avoid overheating, a dwell time between layers was kept constant at 1 minute.

Figure 3.1 – Sample appearance and build-up strategy with path representation.

Commercial pure argon was used in this investigation as shielding gas with a flow rate of 12 l/min. The gas chemical composition is presented in Table 3.3.

Table 3.3 – Shielding gas composition [50].

Gas	Composition [%Vol. abs]	Impurities [ppm]		
Alphagaz 1	Ar	H_2O	O2	C_nH_m
	99.999	<3	<2	<0.5

All parts were built on a mild steel substrate which was cleaned and dried prior to the experiment. All substrates had the dimensions of 250x100x10 mm, in order to obtain

samples with equal building conditions, avoiding distortions and different heat dissipation conditions. The building parameters are summarized in Table 3.4 and are identical to a previous study performed at UNIDEMI.

Table 3.4 – Process parameters (Adapted from [39]).

Sample	Voltage [V]	Current [A]	Wire feed speed [mm/s]	Travel Speed [mm/s]	Heat input [J/mm]
Low heat-input	21	95	3	9	221
High heat-input	21	95	3	3.9	511

Due to supply issues of 1 mm-diameter wire feed stock, and the necessity to proceed with the investigation, fatigue samples were manufactured with 1.2 mm-diameter wire material. This procedure change will be taken into account in the analysis of the results. Table 3.5 summarizes the manufactured samples according to each test to be carried out.

Table 3.5 – Samples identification.

	Test type	Sample	Wire Diameter [mm]
Low heat-input	Uniaxial Tensile Test	1L 2L 3L	1
High heat-input		4H 5H 6H	1
Low heat-input	Fatigue Test	7L 8L 9L	1.2

3.2 Specimens preparation

Once the thin-walled structures production was finished, and before proceeding to the mechanical tests, namely tensile and fatigue tests, several techniques were employed in order to characterize the structures obtained. The main purpose was to guarantee uniformity among each part type and observe the main differences between each part category – low heat-input and high heat-input.

As noted in a previous study [20], this material revealed different behaviour along its height during milling operations. Hence from a macroscopic point of view, the main interest regarding the present study was to evaluate variations of mechanical properties along height. Thus, Figure 3.2 displays the location of each specimen to be removed. Three locations within the walls were individualized, bottom, middle and upper region. Next, samples a), b), c), and d) were extracted using a *GBS-218 Eco AutoCut* saw machine. The first three samples were used for microstructure analysis purposes, whereas sample d) was intended to evaluate the microhardness progression, as well as electrical conductivity along the building direction. Specimens T1, T2 and T3 represent the specimens intended for tensile and fatigue tests. Their preparation and further specifications are detailed in sections 3.4.1 and 3.4.2.

All samples were mounted in epoxy resin and polished to a mirror finish using sandpaper of increasing grades (80-320-600-1200-2500-4000) and for final polishing, a soft *MicroFloc* cloth with 3 μm diamond compound.

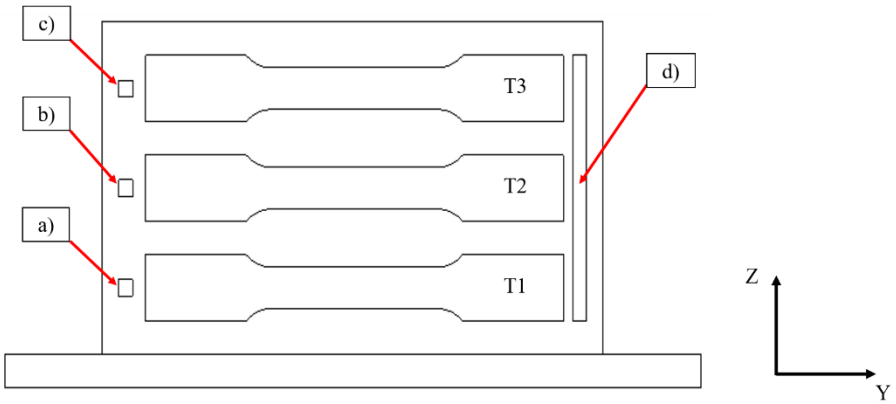

Figure 3.2 – Schematic representation of specimens location used for uniaxial tensile and fatigue testing, and cross-section samples.

3.3 Characterization techniques

3.3.1 Surface waviness measurements

Visual inspection was the first test performed in order to observe macroscopic defects and overall part appearance. Additionally, it allowed to observe and evaluate the surface waviness. Nonetheless, there is a great interest to quantify the surface waviness, as it gives

an understanding on the deposition quality and as well as valuable data that will be used upon machining.

As stated in the literature [51], surface waviness measurements consists in averaging the difference between the maximum wall width, L_m, and the effective wall width, L_e, as illustrated in Figure 3.3. In this way, all samples were scanned, and their surface waviness was assessed using the *DraftSight*® software.

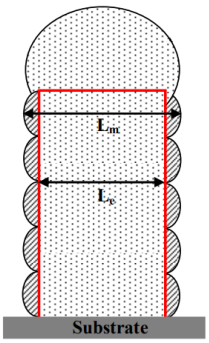

$$\text{Surface waviness} = \frac{L_m - L_e}{2}\ [\mu m]$$

Figure 3.3 – Schematic representation of surface waviness measurements.

3.3.2 Eddy currents testing (ECT)

Eddy current is an NDT technique based on the electromagnetic induction phenomenon. Its main use is to detect surface or sub-surface defects, such as cracks or porosity, on a conductive material based on the change in electrical impedance of a coil of conductive wire.

ECT assesses three different phenomena related to electrical impedance, i.e. material electrical conductivity, magnetic permeability, and probe lift-off. Also, the results are influenced by the frequency that is employed. A lower frequency has a deeper penetration when compared to a higher frequency.

In great conductive materials, as aluminium or copper, there is a greater flow of eddy currents, and hence defects will produce a higher signal. However, ECT signals are considerably affected on ferromagnetic materials due to the increase in flux produced by the significant relative permeability of materials such as carbon, stainless or HSLA steels [52].

Since probe lift-off was held constant, and magnetic permeability has a dominant effect over electrical conductivity given the ferromagnetic nature of HSLA steels, ECT results would show the magnetic permeability evolution along the samples' height.

Tests were performed on samples d), represented in Figure 3.2, on both type of samples. The setup, Figure 3.4, included an *Olympus Nortec 500c* together with an *Olympus* probe of 100 kHz and 300 kHz. For data acquisition, a designed *LabView*® program was used.

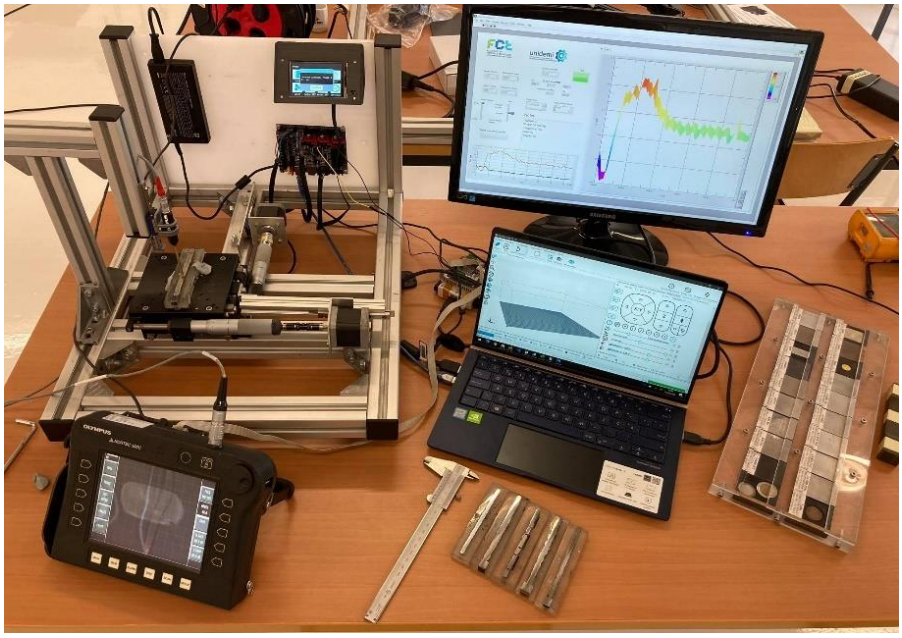

Figure 3.4 – Eddy currents testing setup.

3.3.3 Electrical conductivity measurements

Determining the electrical conductivity is very common both in fabrication and research. Although there are many ways to determine electrical conductivity of a given material, it depends on the type of material, geometry, and method employed. The four-point probe measuring is usually an option, as well as eddy currents. Although both share the same purpose, four-point probe only depends on the electrical conductivity of the material, while the latter takes into account the magnetic permeability of the material, as previously explained.

Electrical conductivity measurement is a complementary technique to microhardness testing. Given the different aspects involved in WAAM processing, such as the multiple layer arrangement or the amount of heat involved with each additional layer, it is essential to assess the electrical mobility variance along the microstructure [53].

Considering the two different wall types produced and analysed in this investigation, it was expected to observe some variation between each sample.

To assess the electrical conductivity of the different samples, the four-point probe method was used, Figure 3.5.

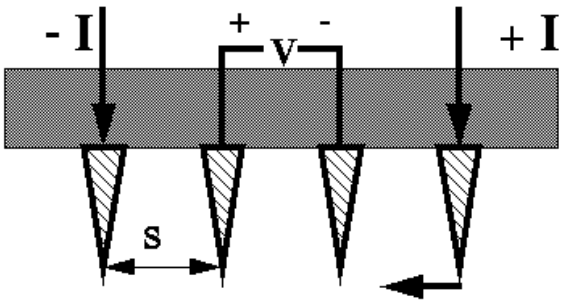

Figure 3.5 – Four-point probe schematic configuration (adapted from [54]).

Thus, tests were performed across the samples' height of 100 mm with a 0.4 mm separation. A standard *Jandel*^{TM} four-point probe was used with a needle spacing of 654 µm and an 80 mA imposed current between the external needles using a *2450 SourceMeter SMU Instrument*.

3.3.4 Microstructure analysis

The properties of a given alloy depend on the corresponding chemical composition and the processing that was subjected, i.e., its thermal and mechanical history. These aspects inflict a given microstructure on the material and will influence its final mechanical properties. In this way, microstructure analysis was performed in order to evaluate the different metallurgical aspects inherent to this manufacturing process as a result of the layer by layer deposition, such as steel phases, grain size and morphology variations along the building direction.

Thus, samples were removed from the bottom (a), middle (b) and upper region (c), embedded in resin, polished and etched with Nital (10% solution). The analysis was then performed using a *Leica DMI 5000 M* inverted optical microscope at CENIMAT/i3N, Materials Science Department of FCT-NOVA.

3.3.5 Microhardness measurements

Microhardness measurements is a destructive technique carried out by successive indentations on a material's sample. It aims to assess hardness variation regarding crystal defects, precipitates and mechanical hardening caused, among other aspects, by the continuous heat accumulation.

As represented in Figure 3.2 all d) samples were removed, embedded in resin and polished. Microhardness tests were performed, according to ISO Standard 6507-1:2018 [55], on a *Mitutoyo HM-112 Micro-Vickers Hardness Testing Machine* available at DEMI-FCT NOVA. A load of 1 kgf for 10 s was selected, across a height of 100 mm, with a separation of 0.5 mm between each indentation along the path represented in Figure 3.6.

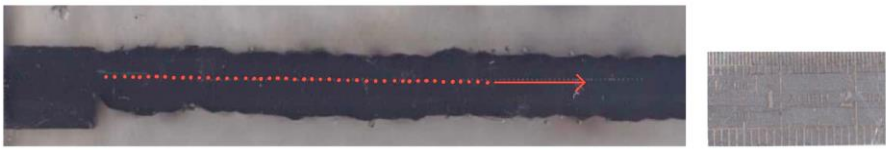

Figure 3.6 – Microhardness measurements path representation.

3.4 Uniaxial tensile and fatigue testing

Once the superficial waviness was removed, all walls were rectified in order to obtain an even thickness and afterwards machine the specimens. As a consequence of process conditions, not all parts were strictly vertical, thus, more material had to be removed in order to accomplish this quest. Hence, low input and high input walls had an average of 2.10 mm and 2.80 mm thickness, respectively.

Longitudinal specimens were extracted from the manufactured walls, as represented in Figure 3.2, by Electrical discharge machining (EDM) at A.J. Maltez – Sociedade Metalúrgica, Lda., using an *ONA AF35* machine. Final specimens are presented in appendix A1.

Prior to testing, surface roughness was measured on a *MarSurf PS10* device and specimens intended for fatigue testing were previously inspected through dye penetrant testing in order to identify any surface-breaking defects.

3.4.1 Uniaxial tensile testing

Uniaxial tensile specimens were designed according to ASTM E8 / E8M-13a, and their corresponding dimensions are depicted in Figure 3.7. Width and thickness of all specimens were measured to obtain the effective area.

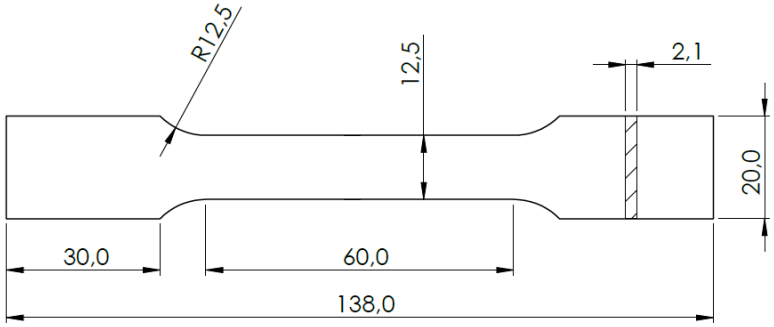

Figure 3.7 – Dimensions of the uniaxial tensile test specimens (low input).

Tests were carried at room temperature using specimens from three low heat-input walls and three high heat-input walls, on an electromechanical *Instron*® testing machine with a load capacity of 50 kN, at Instituto Superior Técnico, as represented in Figure 3.8a). Additionally, strain was measured using a clip-gauge extensometer with a gauge length of 25 mm. The Video Image Correlation (VIC) optical technique was used on the testing of two samples (1L and 4H), in order to obtain a full strain data distribution with higher accuracy, Figure 3.8b). All tests were performed under a cross-head speed of 1mm/min.

a) **b)**

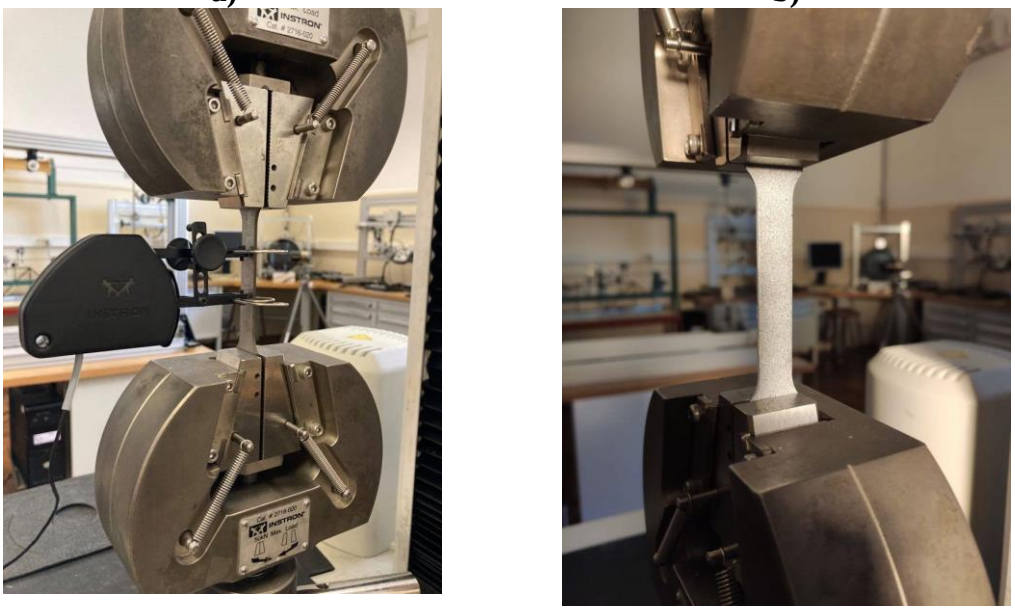

Figure 3.8 – Uniaxial tensile test equipment set-up, a) with clip-gauge extensometer and b) VIC technique.

3.4.2 Fatigue testing

Following the studies carried at UNIDEMI [39] and knowing that higher cooling rates promote the nucleation of acicular ferrite solid solution which is associated with better mechanical properties, namely yield and tensile strength, low heat-input samples were selected to undergo these tests. Thus, nine specimens were extracted from three walls. Specimens were designed according to ASTM E466-15, and their corresponding dimensions are depicted in Figure 3.9.

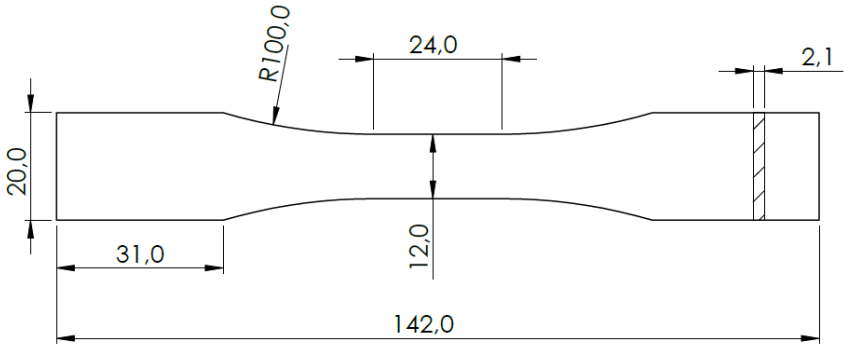

Figure 3.9 – Dimensions of the fatigue test specimens.

Dye penetrant testing were performed, as previously stated, on fatigue specimens. Testing stages are represented in Figure 3.10.

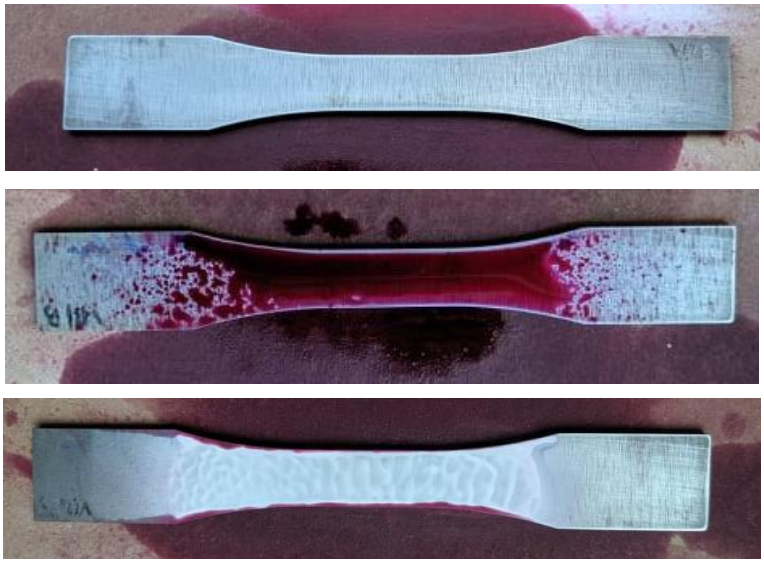

Figure 3.10 – Dye penetrant testing.

Fatigue tests were performed at room temperature, on a servo-hydraulic *Instron® 8502* testing machine with a load cell of 100 kN, at Instituto Superior Técnico, as represented

in Figure 3.11. Loading regime was load-controlled, with a stress ratio of 0.1 (R = 0.1), and sinusoidal constant amplitude with frequency between 12 Hz and 15 Hz. Tests were carried out until specimen's fracture or until they reached 2×10^6 cycles, which were then suspended and considered as run-out. Additionally, a clip-gauge extensometer was placed in the last tested specimen in order to record the strain behaviour with respect to the imposed loading conditions.

After testing, selected fracture surfaces of failed specimens were observed in a scanning electron microscope (SEM) equipped with energy dispersive spectrometry (EDS), to analyse their morphology, the crack initiation region, and the crack propagation mechanisms.

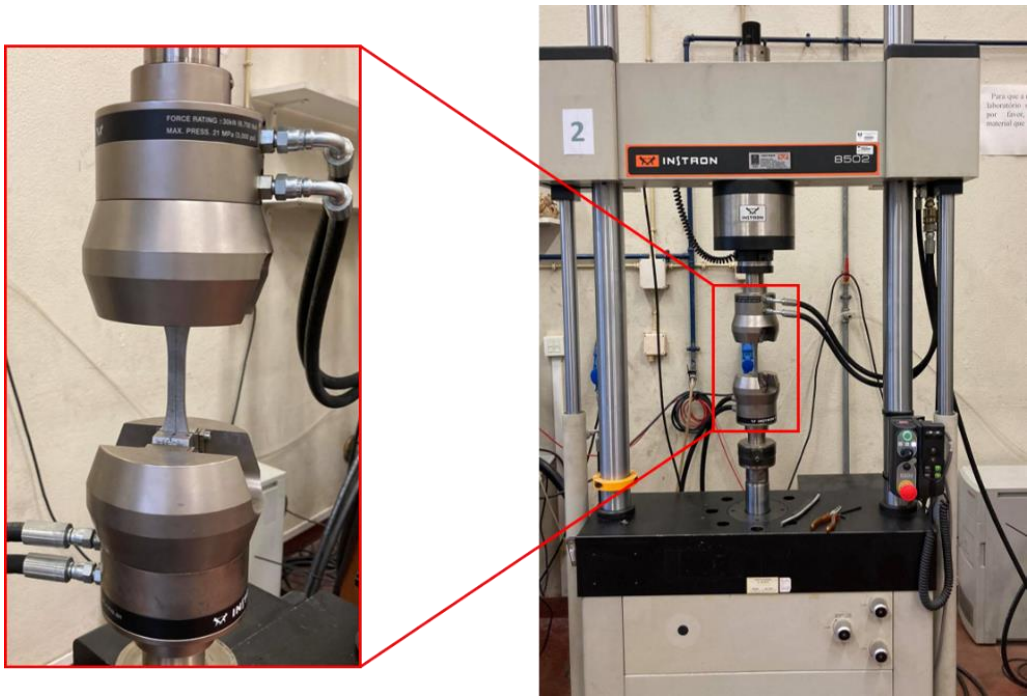

Figure 3.11 – Fatigue test equipment set-up.

3.5 Chapter resume

This chapter intends to outline the essential steps taken in order to conduct the desired experiments. It presents the main information regarding the material that was used, samples manufacturing procedure and specimens preparation. Additionally, all characterization techniques and mechanical tests were described, as well as the required equipment. The results obtained from the experiments are presented and discussed in the following chapter.

4 Results and Discussion

4.1 Macroscopic characterization

On one hand, the fastest travelling speed used to produce the low heat-input samples led to less dilution as well as less penetration between each layer. This resulted in thinner parts compared to high heat-input samples as can be observed in Figure 4.1.

On the other hand, using a lower speed with the same process parameters gave rise to less penetration in the previously deposited layer, increasing the fusion pool, which in turn resulted in wider samples. The required height was achieved with less layers, approximately 70 compared to 90 observed for low heat-input samples, which contributed to reduce the manufacturing time.

With high heat-input, despite an increased wettability during lower speeds, it was observed higher waviness results. One possible reason may be ascribed to the greater material volume present in this variant. It was also observed in both samples presented in Figure 4.1 a) and b), that the first layers presented a narrower bead width, which occurred because of the fast cooling rate that took place at the beginning of the manufacturing process. The waviness and width average values of each sample type are presented in Table 4.1.

Figure 4.1 – a) High heat and b) low heat-input cross sections.

Table 4.1 – Waviness and width average values of each sample type.

Sample	Waviness [μm]	Width [mm]
Low heat-input	597 ± 88	4.9 ± 0.2
High heat-input	660 ± 143	8.2 ± 0.3

In addition, all manufactured parts were exempt of superficial defects. However, the substrate revealed great amount of distortion due to the amount of heat developed during processing. This feature may be a result of significant accumulation of residual stresses, which should be taken into consideration when analysing the mechanical properties results.

4.2 Microscopic observations

The cross-section macrostructure of the low heat-input samples and the high heat-input samples is presented in Figure 4.2 and Figure 4.3, respectively. From Figure 4.4 and Figure 4.5 it is possible to observe, with greater detail, the microstructure evolution along the wall's height for both type of heat input samples.

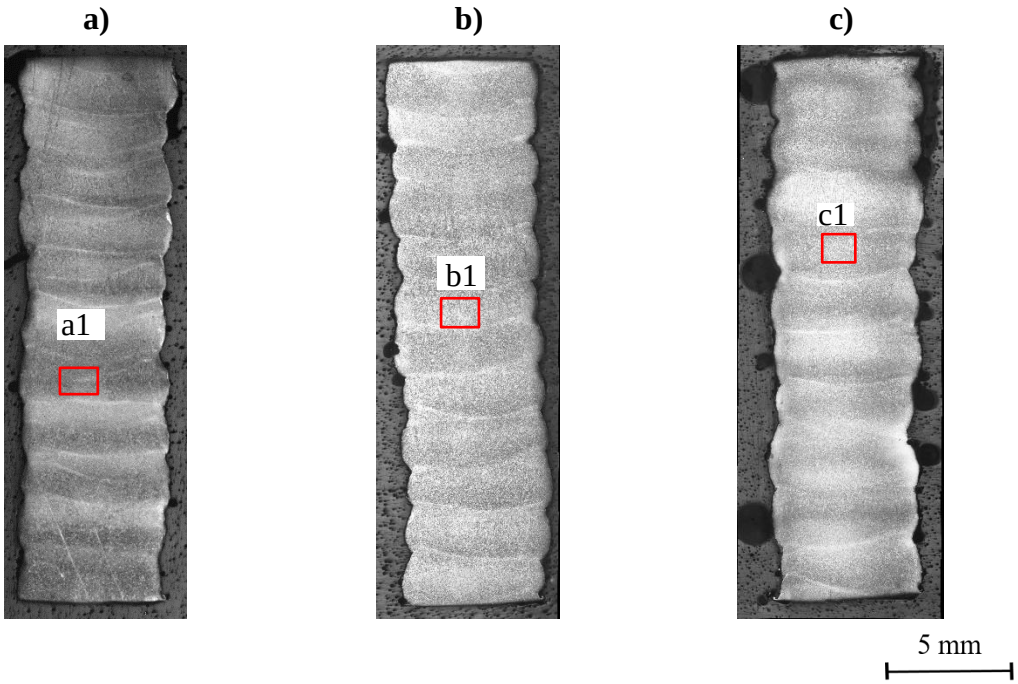

Figure 4.2 – Macrographs of low-input samples across a) bottom, b) middle and c) top region.

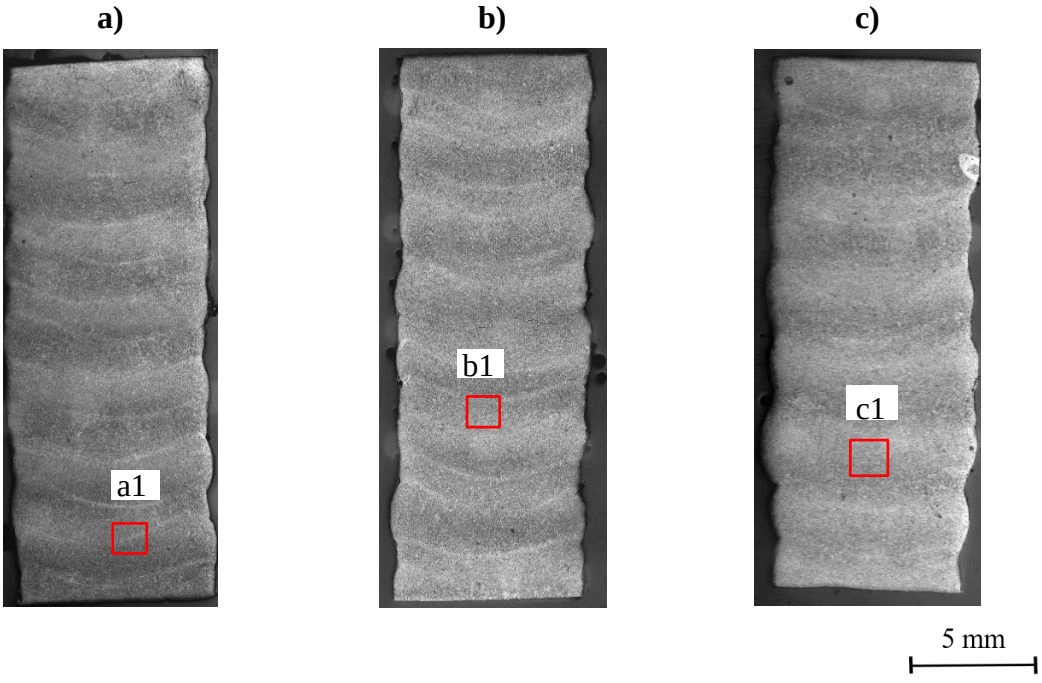

Figure 4.3 – Macrographs of high-input samples across a) bottom, b) middle and c) top region.

Low heat-input

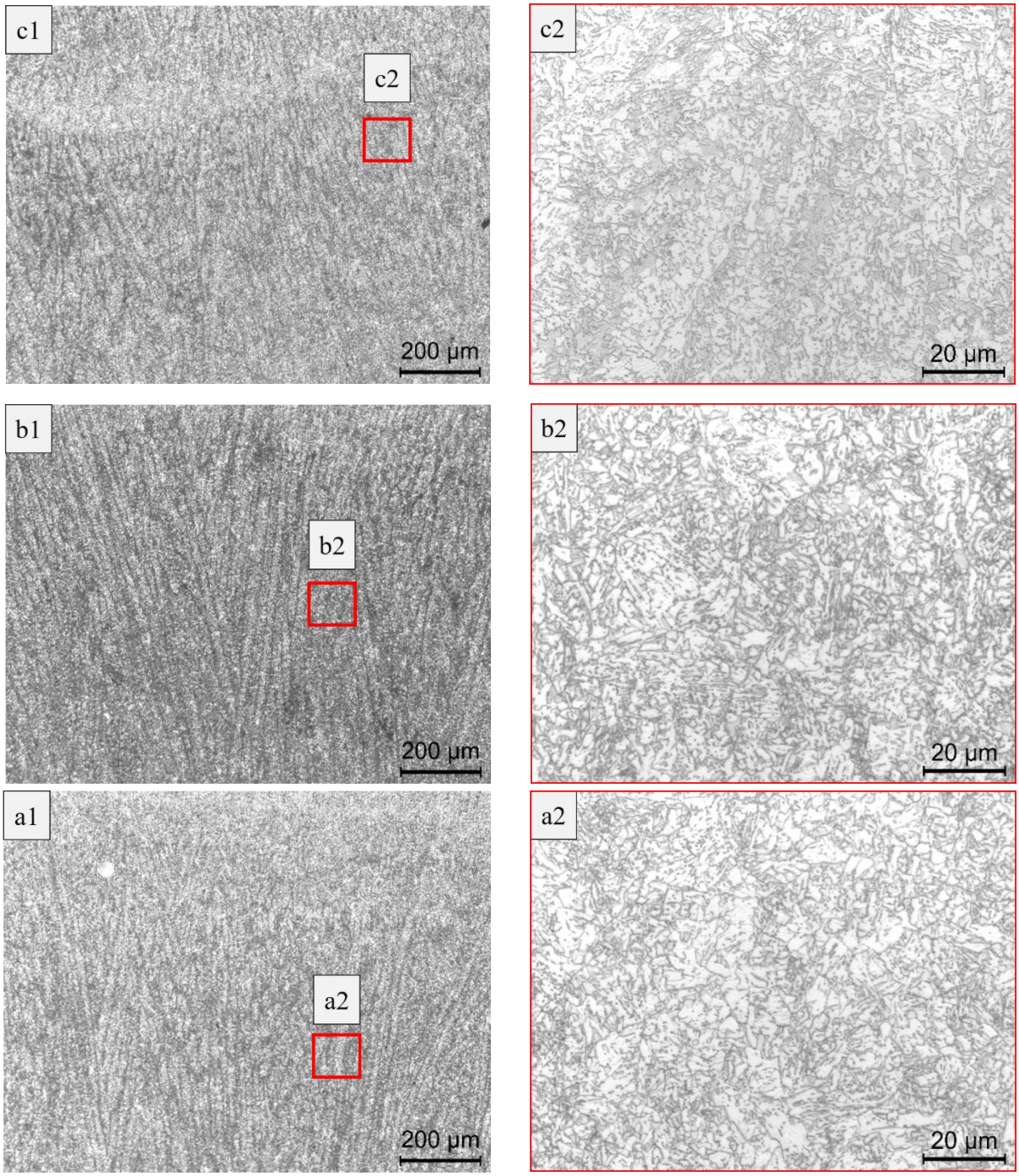

Figure 4.4 – Microstructure observations of low heat-input samples in different wall regions, 10x and 100x magnification, left and right, respectively.

High heat-input

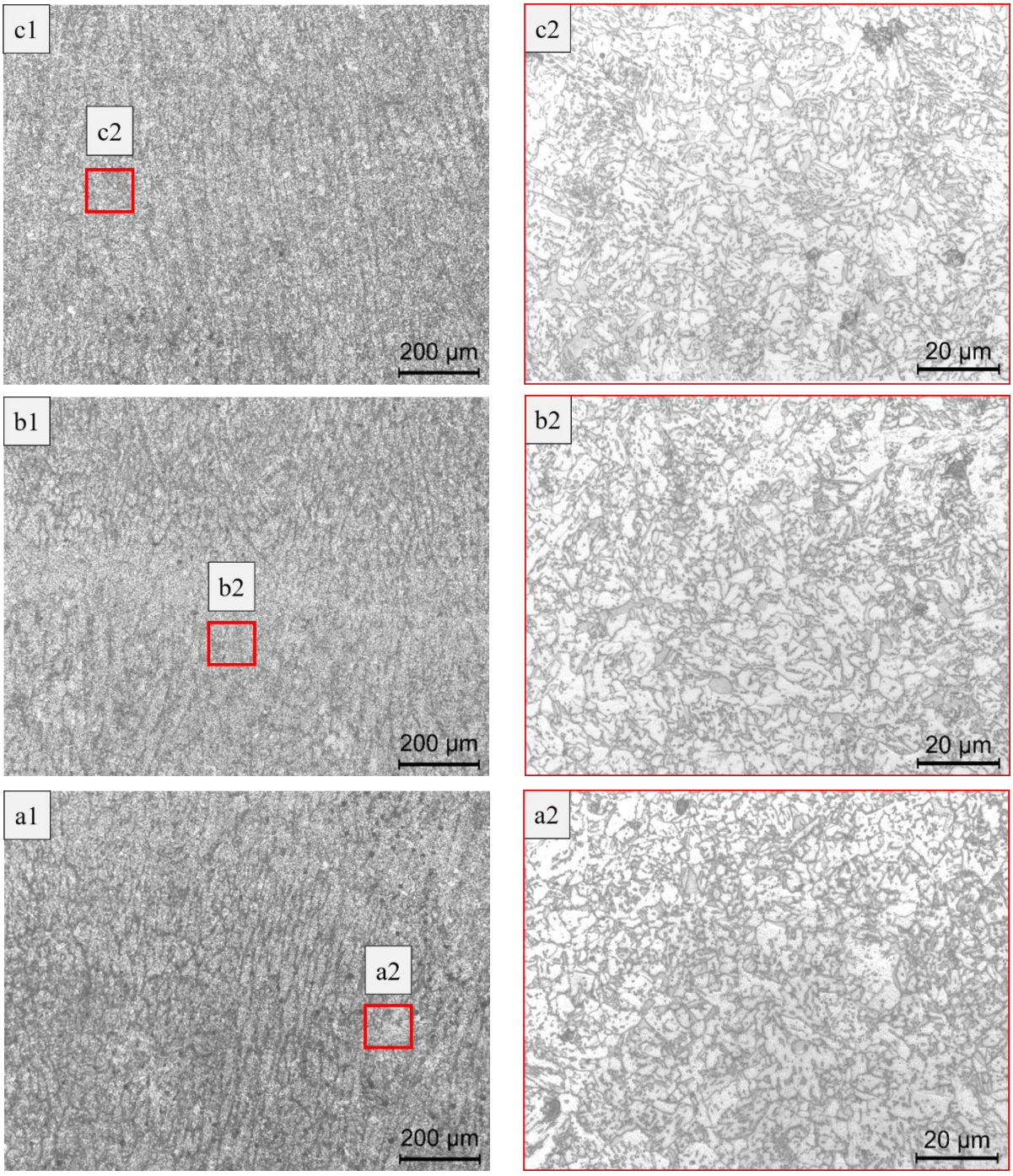

Figure 4.5 – Microstructure observations of high heat-input in different wall regions, 10x and 100x magnification, left and right, respectively.

The main constituents of this HSLA steel are a mixture of gamageneous and alphageneous elements, i.e., elements that increase the interval of austenite (Ni, Mn) and ferrite (Cr, Mo, Si) solid solutions, respectively [56]. Hence, the columnar morphology observed in the micrographs presented in both Figure 4.4 and Figure 4.5, corresponds to

the solidification that took place initially, where the dominating microstructure is austenitic. Subsequent cooling led to ferrite formation from the austenite grain boundaries. This process repeats itself with each adding layer. Therefore, during manufacturing the microstructure experienced back and forth austenite and ferrite transformations. The final microstructure is comprised mainly of pearlite and ferrite. In addition, bainite or acicular ferrite are some of the solid solutions that took place. The nucleation of intragranular acicular ferrite, particularly, contributes to increase the material resistance and toughness [57]. However, it is important to note that the optical microscopy hinders the presence of other microconstituents, which otherwise would be visible by SEM, for example. Thus, further analysis on the microstructure of this material and its constituents can be found in the investigation performed by Rodrigues *et al.* [39].

As previously stated, microstructural analysis showed columnar grains oriented along the building direction with a clear inclination preference towards the centre. This aspect can be explained by the cooling effect that occurred from the edges towards the centre of the wall, Figure 4.6. As the layer edge is approached, a remelting zone is visible, resulting in a discontinuity on grain distribution and finer microstructure, e.g. Figure 4.4 c1). Depending on the ability of dissipating heat, the columnar grain may present higher or lower width, and this aspect differs from high to low heat-input samples. However, this is a two-dimensional analysis, and as such, even though columnar grain morphology was observed, it is not possible to assess their precise orientation within the wall. Spatial grain disposition will influence aspects such as mechanical properties (Young's modulus and tensile stress) and/or machining performance, thus, for this purpose Electron Backscatter diffraction (EBSD) analysis should be performed.

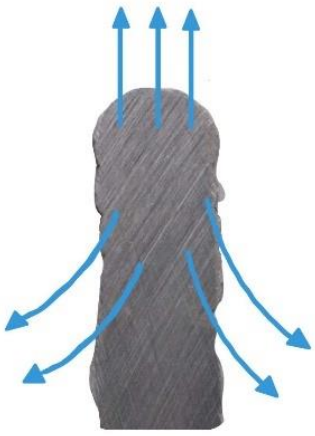

Figure 4.6 – Schematic representation of the cooling flow.

Within each wall, all the samples analysed revealed finer microstructure at the bottom and the top when compared to the middle region. Therefore, grain size was observed to increase along the building direction and decrease towards the top region. With each additional layer, the building sample experienced a decrease in thermal cycles, and thus, the temperature in the middle section was kept at a higher level for a longer period of time, which allows to explain the courser grain observed [47].

When different heat-input microstructures were compared, high heat-input samples revealed an overall slight increase in grain size due to the lower cooling rates that these walls were subjected. Additionally, lower heat-input is associated with higher cooling rates, which consequently increases heat gradients and leads to finer microstructure compared to high heat-input walls. Moreover, cooling rates on both type of samples were not low enough to cause the formation of brittle and hard microstructure such as martensite.

Nonetheless, the grain size increase, on all observed samples, did not seem to be significant, which led to assume that the equal cooling time in between layers may have a more profound effect on grain growth than the heat input. Although layers on high input walls always started at a higher temperature, the dwell time influence the extent to which the material is able to accommodate and experience grain growth, as in an equilibrium situation. Another approach to compare different heat input microstructures would be by starting the deposition always at the same temperature despite still having different welding speeds.

4.3 Eddy currents testing

Adding to the aforementioned characterization techniques, eddy currents testing was carried out. As mentioned in section 3.3.2, this NDT technique measures the material's electric impedance. Thus, any significant change in the material properties or the presence of defects along the building direction should reflect a fluctuation on the eddy current signal.

The tests performed on low heat-input samples were more difficult to conduct than those on high heat-input samples. The reason that explains such difficulty is the flow distortion experienced due to the edge effect that prevails on the narrow width profile,

given that the probe diameter was approximately the same size as the profile width. Nonetheless, a similar trend was observed on both heat-input samples. The ECT result of a high heat-input sample is presented in Figure 4.7.

In spite of the significant amount of noise, from Figure 4.8 (low heat-input sample), it is possible to observe a clear signal trend as the probe progresses throughout the sample. Given the substrate penetration during the first layer deposition along with the added temperature, a ramp progression is observed instead of an abrupt variation. One may conclude that when compared with the base material, all samples present a lower magnetic permeability. Another conclusion is that in the presence of unvarying conditions, the magnetic permeability tends to remain uniform. However, regarding 5H sample result, presented in Figure 4.7, the few substantial variations noted, especially near the 55 mm distance, can be attributed to two different reasons. One may be a pore defect located on the sub-surface region. The other may be attributed to the change of inter-layer cooling time on that particular region. In other words, during the manufacturing process the machine was interrupted due to technical issues, which could allow for a dwell time higher than one minute, resulting in a longer cooling period. The next layers were subjected then to different temperature conditions which led to changes in the microstructure and consequently on magnetic permeability of the material.

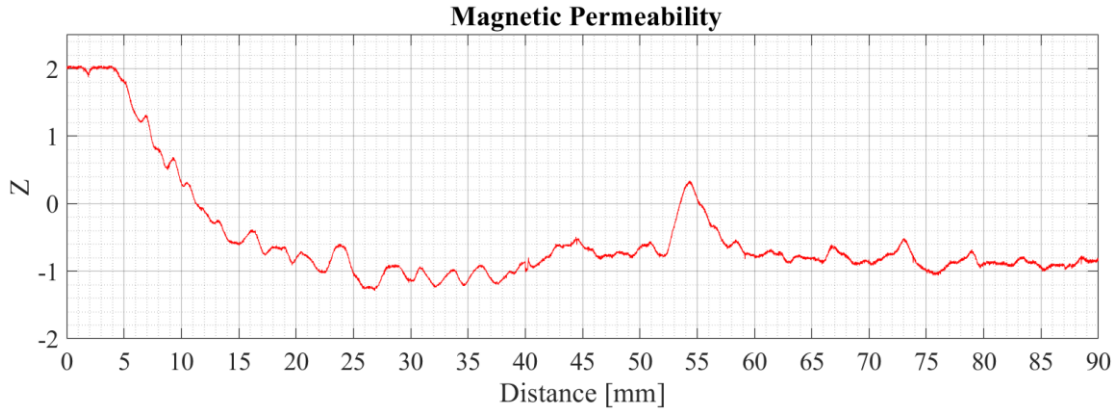

Figure 4.7 – Eddy currents testing result on 5H sample with 300 kHz.

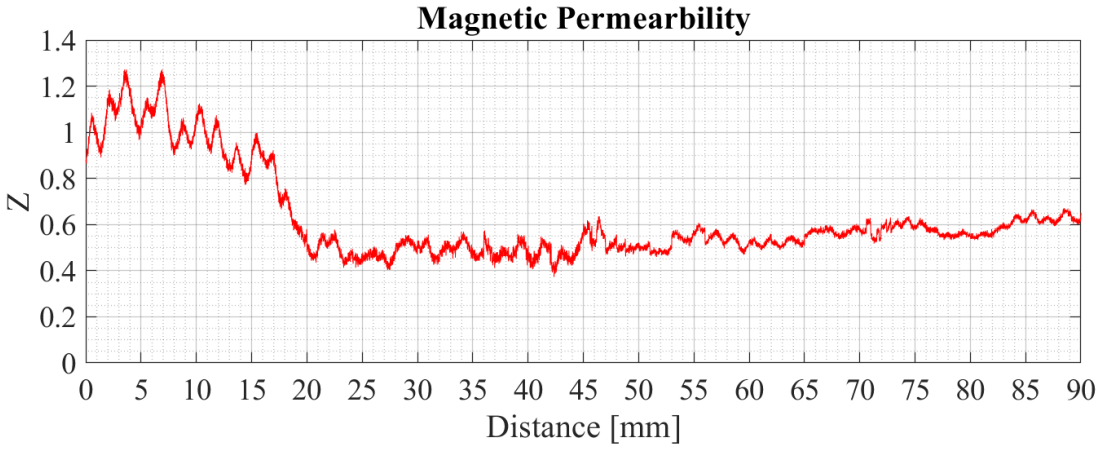

Figure 4.8 – Eddy currents testing result on 3L sample with 100 kHz.

The results obtained by ECT were consistent among the many samples that were tested and regardless the selected frequency. It is important, however, to complement the data with the other techniques in order to attain a larger perspective concerning material properties of these samples, especially 5H sample, to understand the signal variance that was observed in this section.

4.4 Electrical conductivity measurements

Electrical conductivity results carried out by the 4-point probe are presented in Figure 4.9. The results are expressed in International Annealed Copper Standard (%IACS) and represent the ability of a given material to conduct electrical current when compared to copper. As expected, a transition may be observed as the probe progresses from the substrate towards the first layers, given the heterogeneous properties between the two materials. In addition, low heat-input samples demonstrated a lower electrical conductivity profile of about 3% IACS. Such behaviour may be explained due to the fewer thermal cycles these samples were subjected to, which originated a smaller grain size as already observed in section 4.2. High heat-input samples see an increase in grain size, with reduced grain boundaries which benefits the electrical current flow. Furthermore, towards the end of both walls, a slight increase of electrical conductivity was observed.

Steel's electrical conductivity is known to range between 3 – 15 % IACS. In this case, the HSLA parts showed an average conductivity between 3 – 3.5 % IACS, which is well

represented for this kind of steels, that generally presents lower electrical conductivity. The presence of 1.7 % of manganese and 2% of nickel are not only responsible for increasing the hardenability, strength, or ductility, but also produce a significant effect on electrical resistivity [58].

Throughout all electrical conductivity profile, a zig-zag pattern was observed. A closer look, depicted in Figure 4.9 b), shows that there is an average close to 1 mm distance between each peak. The distance between each deposited layer is about 0.8 mm to 1.2 mm. One possible explanation, that will require further investigation, may be ascribed to the difference in microstructure that exists in-between two consecutive layers where the remelted zone experienced an annealing treatment, as seen in section 4.2. As the probe approaches the layer interface, the presence of different solid-state solutions leads to microstructure variations and decrease in grain size as stated before, which consequently decreases the electrical conductivity. Hence, from layer to layer, there is a small fluctuation in electrical conductivity, expressed by the scatter observed in Figure 4.9 [53].

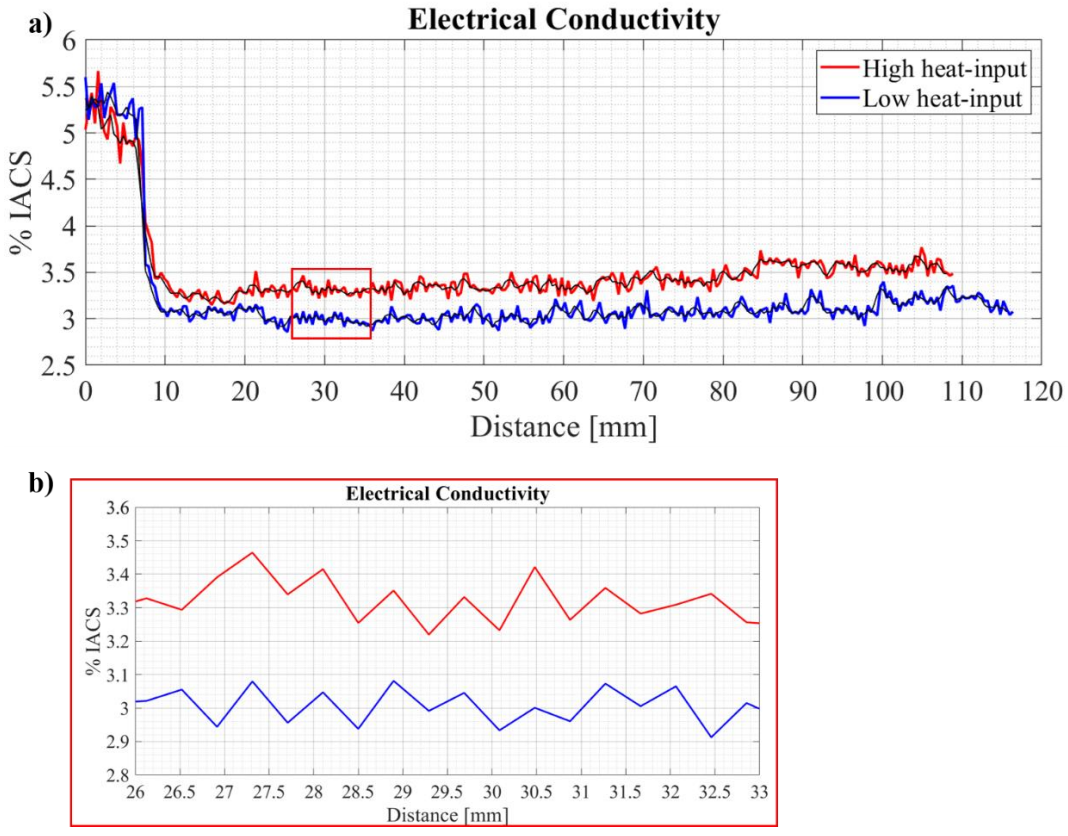

Figure 4.9 – (a) Electrical conductivity along height and (b) detailed observation of 3L and 6H samples.

Regarding 5H sample, its result is depicted in Figure 4.10. It is possible to detect a slight variation of electrical conductivity, especially from 30 mm distance onwards. Although the small variation may be negligible, it is necessary to take it into account in order to understand the variation observed in ECT testing. Microhardness measurements will provide further insight concerning this sample.

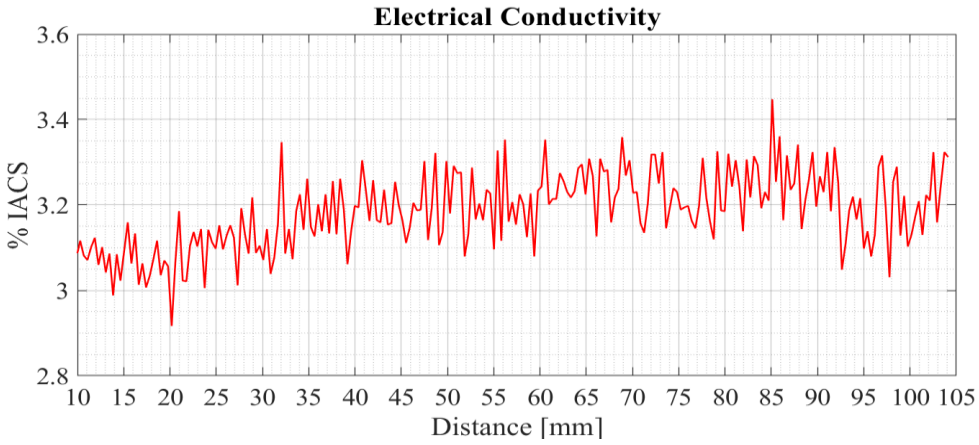

Figure 4.10 – Electrical conductivity of 5H sample.

Four-point probe testing revealed to be a complementary analysis of eddy currents testing when ferromagnetic materials are concerned. Both profiles showed a similar path trend, which allows to conclude that in the presence of uniform conditions during processing and the absence of structural defects, such as pores or inclusions, there is a uniform variation along samples' height, regardless the input energy.

4.5 Microhardness results

Microhardness measurements showed different results as far as energy input is concerned. Using the same wire diameter, low heat-input samples presented a harder microstructure than high heat-input samples. This result may be explained by the increase in heat accumulation and larger grain size present in the latter. However, for 1.2 mm wire, and same process parameters, a significant decrease in microhardness was observed, and a possible explanation is the decrease in energy density experienced with this wire diameter. Average microhardness values are presented in Table 4.2 and all microhardness profiles can be found in appendix A2.

Moreover, it is possible to observe a visible evolution pattern along the material's height, Figure 4.11. All samples start from a higher microhardness value and decrease close to the middle, only to start increasing again near the top. This variation in microhardness values between the different wall regions may be attributed to the effects of thermal histories on the mechanical behaviour [39, 58]. As stated in the literature, the temperature stabilizes from a certain layer that is located near the middle region. In this way, the first layers, the middle and upper regions experience different thermal cycles effects, which influence grain size, as well as phase formation processes. Thus, in uniform process conditions, i.e., exempt of any stops, it is possible to conclude that hardness decrease in the middle section suggests an increase in material ductility due to more pronounced heat accumulation experienced when compared to bottom or top regions.

Table 4.2 – Microhardness average values.

Load (g)	Low heat-input (1 mm)	High heat-input (1 mm)	Low heat-input (1.2 mm)
1000	327 ± 14 HV	277 ± 9 HV	248.2 ± 12.5

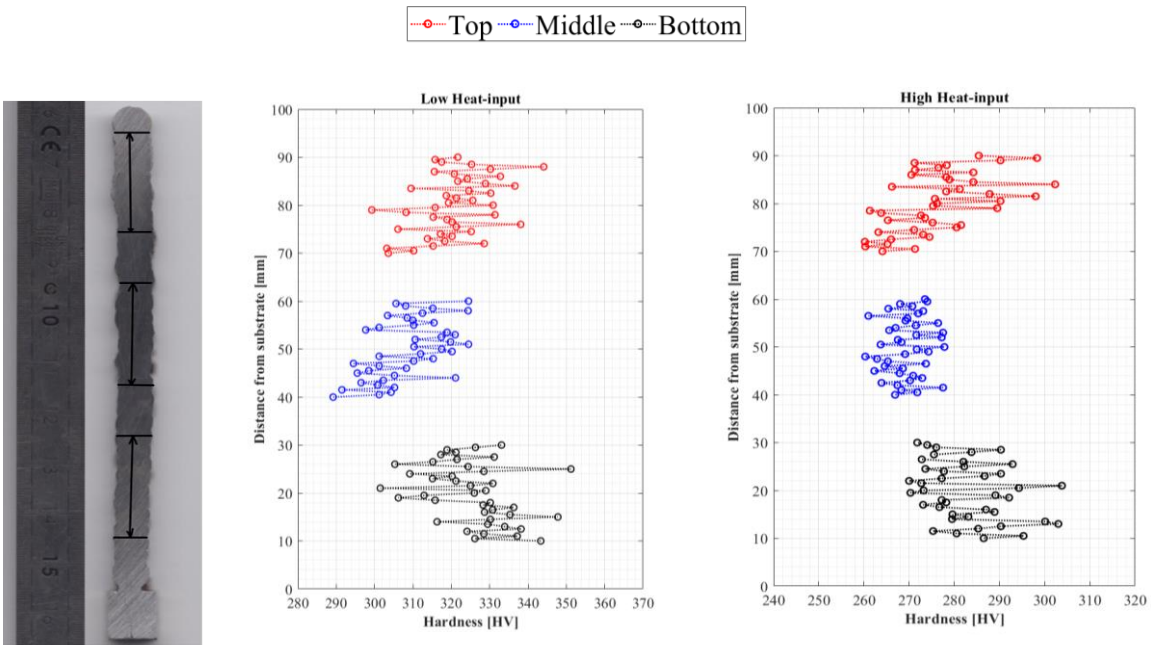

Figure 4.11 – Microhardness measurements along specimens height (3L and 4H).

Following the observations made on the 5H sample on the previous sections, the microhardness profile is represented in Figure 4.12a). Contrary to the remaining profiles,

this sample does not show a hardness decrease in the middle region or a similar increase in the top region. It is possible to conclude that regardless the existence of a material defect, the different results are a consequence of a change in microstructure due to an increased dwell time in-between layers. The subsequent layers experienced cooler conditions, almost similar to the bottom region, which resulted in smaller grain size and thus, increased hardness.

Another important aspect concerning this testing is the hardness variation along the layer, which is presented in more detail in Figure 4.12b) for 3L sample in the middle region. A significant decrease in hardness is visible near the layer boundary. Whereas the maximum hardness value is obtained in the mid layer region. This feature may be explained by the following: after the last deposited layer, the outermost region experiences a faster cooling rate, as displayed in Figure 4.6, which resulted in a harder microstructure. However, when the next layer is deposited, it partially remelts the previous one and in addition, it acts as a heat treatment. This annealing effect causes finer microstructure in that region and decreases the interface microhardness. This is an important aspect to understand, since there is not only variation along the height, but also from layer to layer and within the layer. This aspect may influence, for example, the mechanical properties whether the specimen is extracted crosswise or lengthwise.

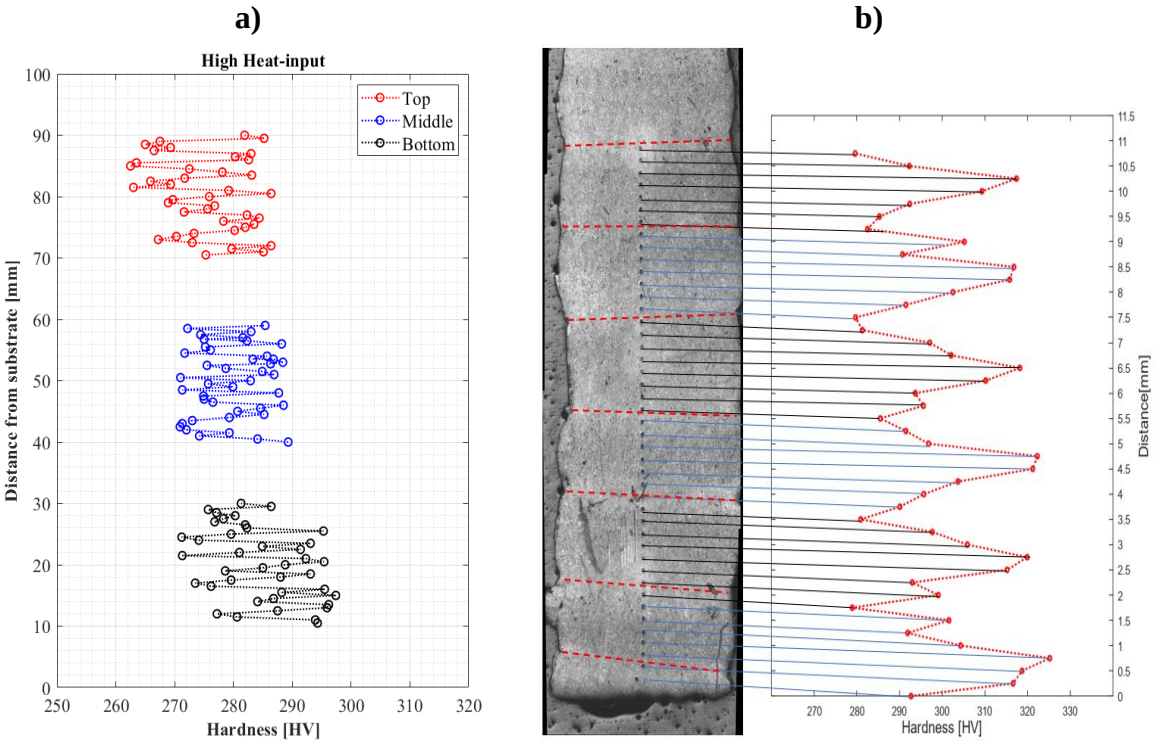

Figure 4.12 – a) Microhardness profile of 5H sample and b) detailed layer observation of 3L sample.

This testing is based, as mentioned, on discrete indentations in the mid thickness wall area and is influenced by local phase formation regions, precipitates, or surface defects. Therefore, it is evident that the results obtained may not capture other fine microstructural details. This explains the complementarity to the previously performed NDT techniques. The scatter visible in the other plots can be explained by the result obtained in Figure 4.12b). Given that each indentation had 0.5 mm spacing, it could easily capture either a layer interface or a non-affected region.

4.6 Uniaxial tensile testing results

Low heat-input and high heat-input specimens presented an average roughness (Ra) of 1.35 μm and 1.66 μm, respectively. Ra and Rz results for each specimen can be consulted in appendix A3.

After performing the uniaxial tensile tests, all the results were processed in order to obtain the adequate stress-strain curve for each specimen. Given the difficulty to identify the stress at which the material changes from elastic to plastic behaviour, the 0.2% offset yield strength was determined. A line parallel to the elastic regime was traced, as depicted in Figure 4.13, with an offset of 0.2% and its intersection with the stress-strain curve corresponds to the 0.2% offset yield strength of the material. Note that the slope (Young's modulus) was adjusted between 200 GPa and 210 GPa. It was observed, however, that a slight change in the line's slope would not incur in major variance regarding the aforementioned strength.

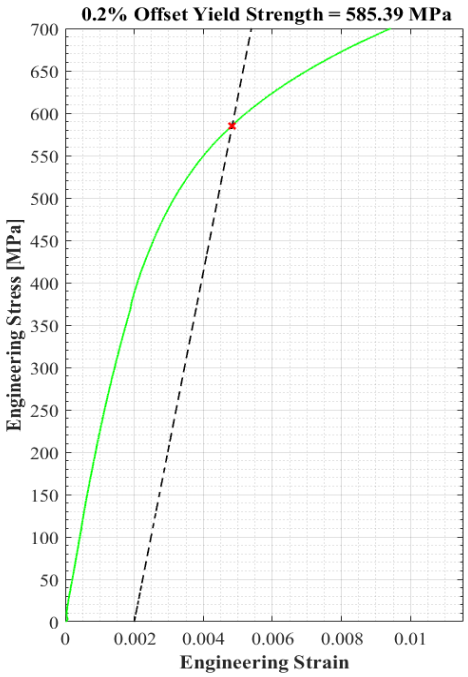

Figure 4.13 – Offset YTS representation.

All specimens presented a ductile fracture due to an increased plastic deformation with a subsequent decrease in cross-sectional area. Figure 4.14 shows 3L (a) and 4H (b) specimens after testing.

a)

b)

Figure 4.14 – Fracture location after testing on a) 3L and b) 4H (VIC) specimens.

Ultimate tensile strength (UTS) values ranged between 860 MPa – 950 MPa, which was similar to material's datasheet [49], 940 MPa – 980 MPa. Data sheet values for yield tensile stress (YTS) present a range of 880 MPa – 920 MPa, however, the results obtained from the tests were considerably lower, 530 MPa – 620 MPa, resulting in an average decrease of 35 %. YTS and UTS results can be observed in Figure 4.15 and Figure 4.16, respectively.

The YTS decrease infers that this process, with this steel material, diminishes its ability to recover after experiencing tension stresses and consequently suffers a faster transition from elastic do plastic deformation.

It is important to note, however, that not all specimens fractured within the clip gauge measuring length, as observed in Figure 4.14a), which adds to the conclusion that important elongation was not measured after necking occurred. This aspect was possible to overcome by performing tests using VIC on specimens 1L and 4H.

Additionally, in these tests, stress was applied perpendicularly to grain distribution (assuming that grain layout is predominantly in the vertical direction as was observed from microscopic analysis), and as a result, different behaviours should be expected, especially as far as ductility and UTS are concerned. This feature was already reported in WAAM literature, for example in Refs. [47, 56].

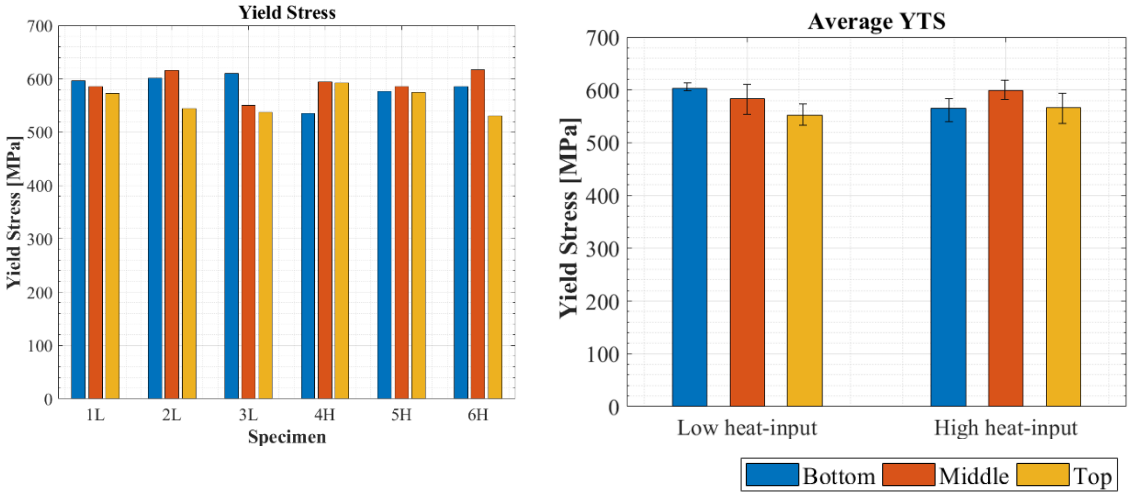

Figure 4.15 – Yield Stress (YTS) and the corresponding average value (right).

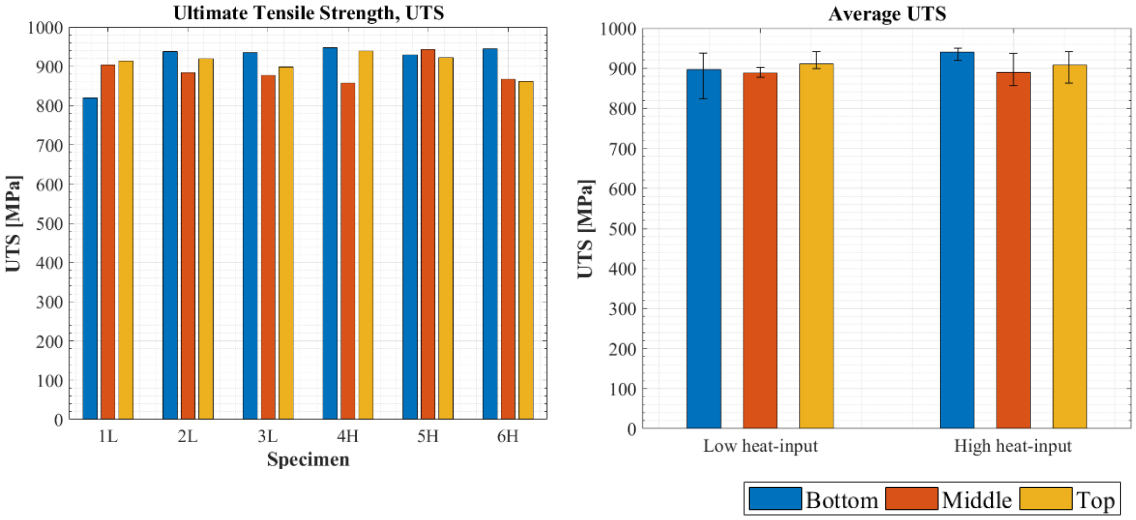

Figure 4.16 – Ultimate Tensile Strength (UTS) and the corresponding average value (right).

From Figure 4.15 is observed that YTS does not present a significant or straightforward pattern between the different heat-input specimens. YTS on low heat-input specimens decreased on average along the building direction, whereas on high heat-input the middle section presented the higher YTS value. Although it decreased globally compared to the material data sheet, as mentioned previously, it is not possible to establish a direct link between heat input or wall region and the YTS of the material. Although it is possible to observe a decrease along height on low input specimens, this is contradicted by the high input specimens. Another important aspect that potentially masks the results is the presence of surface and internal defects. Thus, as far as these results are concerned,

it is possible to assume that YTS does not vary significantly with respect to energy input and wall region.

On the other hand, UTS is slightly higher in the bottom and top tested specimens. This aspect can be explained by the increased hardness that was noticed in the first and last layers. As such, the lower value of UTS is found to be in the middle, as expected, following the microhardness profile pattern. Specimens from 3L wall represent very well this characteristic since no significant stops occurred during manufacturing. Contrary to 3L, 5H wall presented a small UTS increase in the middle region, which is verified by the microhardness profile already explained and presented in Figure 4.12a).

Moreover, from the stress-strain curves presented in Figure 4.17, the lower strain displayed by the upper specimen of 5H wall should not be representative of that region, nor the material, since subsequent fracture analysis displayed the presence of pores, which were responsible for the premature fracture, as observed in Figure 4.18a).

A first glance on 3L stress-strain curves shows that greater ductility was achieved in the middle region. Since hardness and ductility are inversely related, it is possible to assign this behaviour to the microhardness profile that was already mentioned. The observations made from this wall are in agreement with the fracture surface analysis, Figure 4.18b), which revealed the presence of dimples, denoting ductile fracture.

Nonetheless, it is essential to bear in mind that material hardness should not be the only property to look at. Internal defects, manufacturing conditions or even specimens preparation should be taken into account and can also explain the different patterns observed in the stress-strain curves presented in Figure 4.17. This aspect was verified on testing using VIC, where 1La and 1Lb specimens displayed significant elongation due to the absence of any defect. On the other hand, all 4H specimens displayed premature fracture due to surface pores, as indicated by the arrow in Figure 4.19.

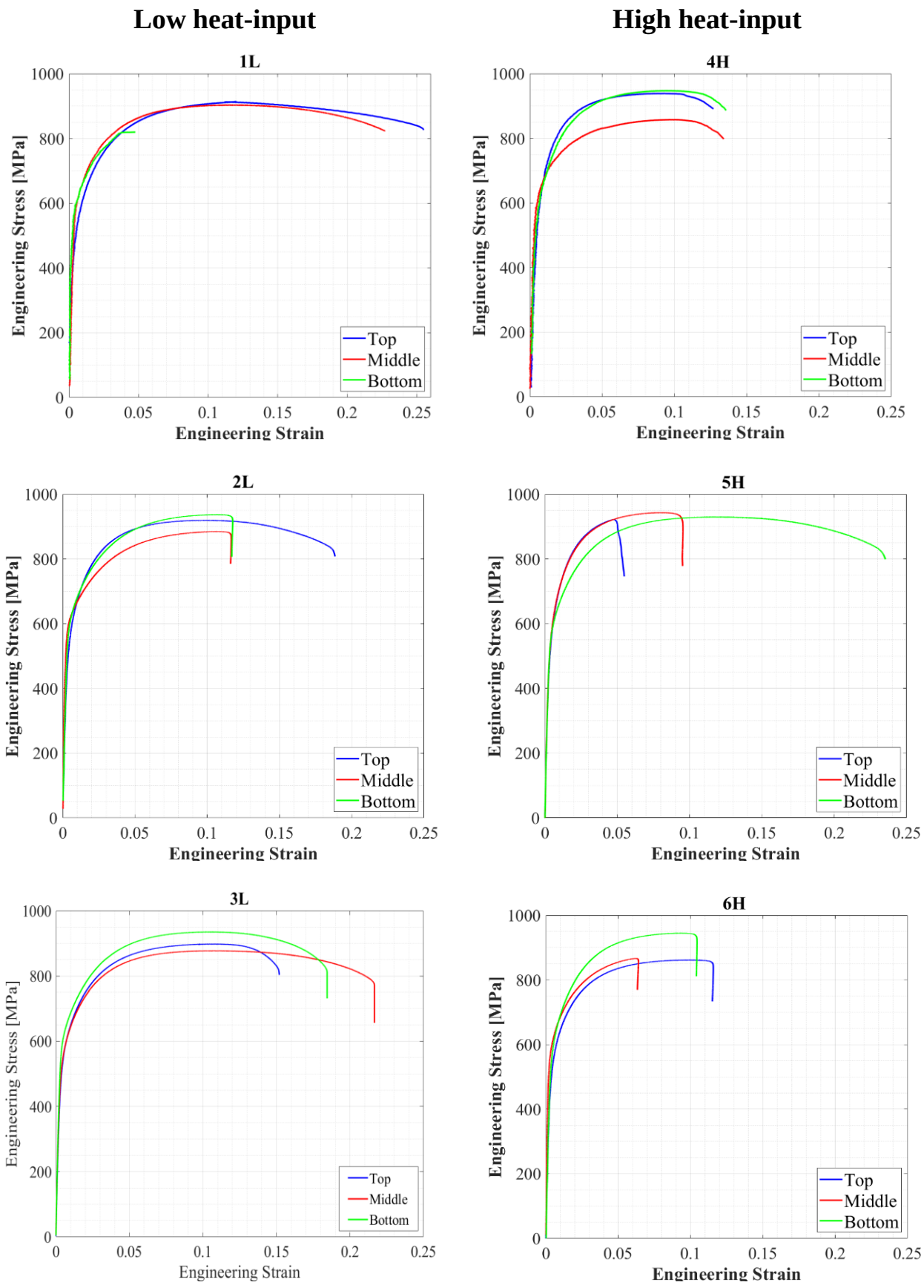

Figure 4.17 – Stress - Strain curve of low heat-input (1L, 2L and 3L) and high heat-input specimens (4H, 5H and 6H).

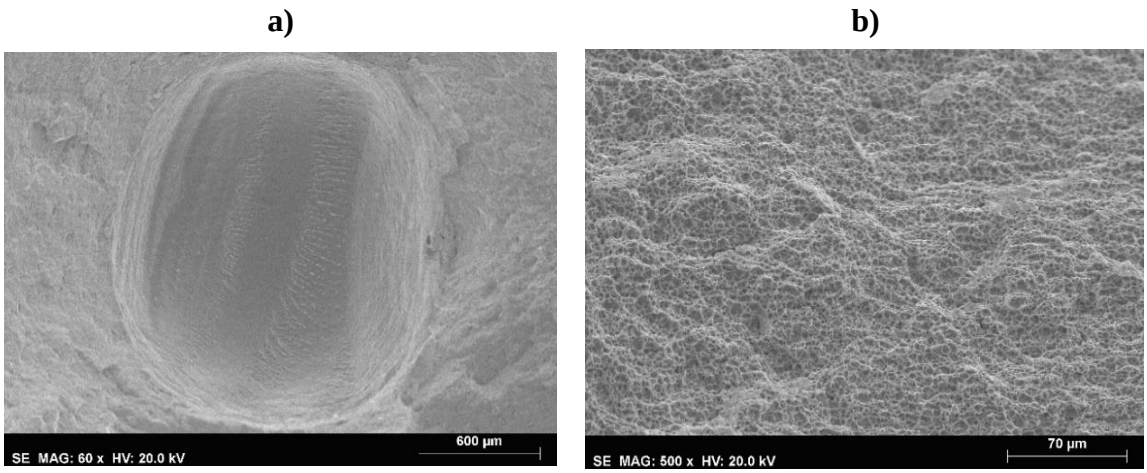

Figure 4.18 – Fracture surface features of a) 5Hc and b) 3La specimens.

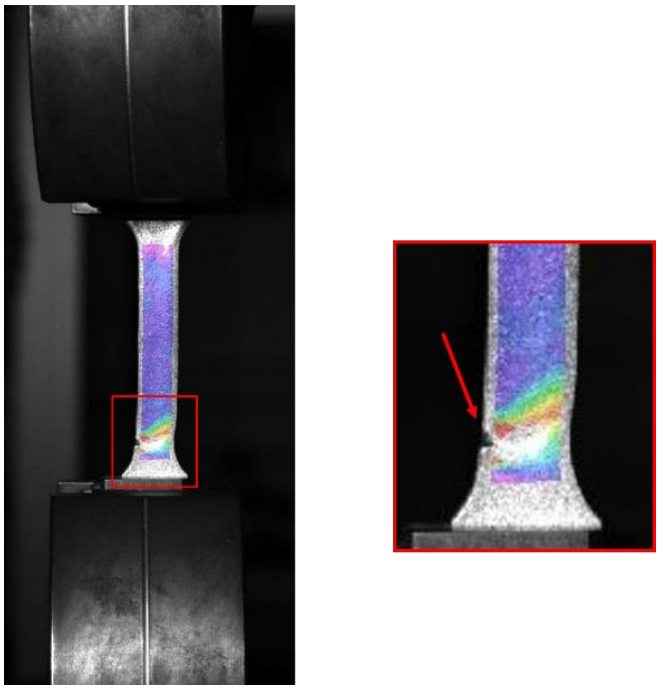

Figure 4.19 – Representation of a surface pore defect that induced premature fracture on sample 4Hb.

Additionally, resilience and toughness modulus were calculated for each specimen. Resilience modulus, U_r, can be defined as the energy absorbed by the material under elastic load, or in other words, the energy necessary to enter in the plastic regime. Thus, resilience is represented by the area under the elastic region and is given by equation (4.1), where σ_y and ε_y, represent stress and strain values at yield point, respectively. Using the simplification presented by equation (4.2), resilience modulus was calculated, and the results are presented in Figure 4.20.

$$U_r = \int_0^{\varepsilon_y} \sigma d\varepsilon \tag{4.1}$$

$$U_r = \frac{1}{2}\sigma_y \varepsilon_y = \frac{1}{2}\sigma_y \frac{\sigma_y}{E} = \frac{{\sigma_y}^2}{2E} \tag{4.2}$$

On the other hand, toughness modulus, U_T, by definition, is the required energy to reach final fracture. It is calculated by the area under the stress-strain curve, given by equation (4.3), where ε_f represents strain value after fracture.

$$U_T = \int_0^{\varepsilon_f} \sigma d\varepsilon \tag{4.3}$$

It is important to understand whether there is variation regarding toughness from low input to high input specimens, or along samples height. Usually, for the same UTS, greater toughness modulus is associated with greater ductility, which is the ability to undergo plastic deformation before fracture.

The modulus of toughness was calculated, as the previous properties, with *MATLAB* software, using the *trapz()* function, which can deliver an approximate value of this property. The results are presented in Figure 4.20.

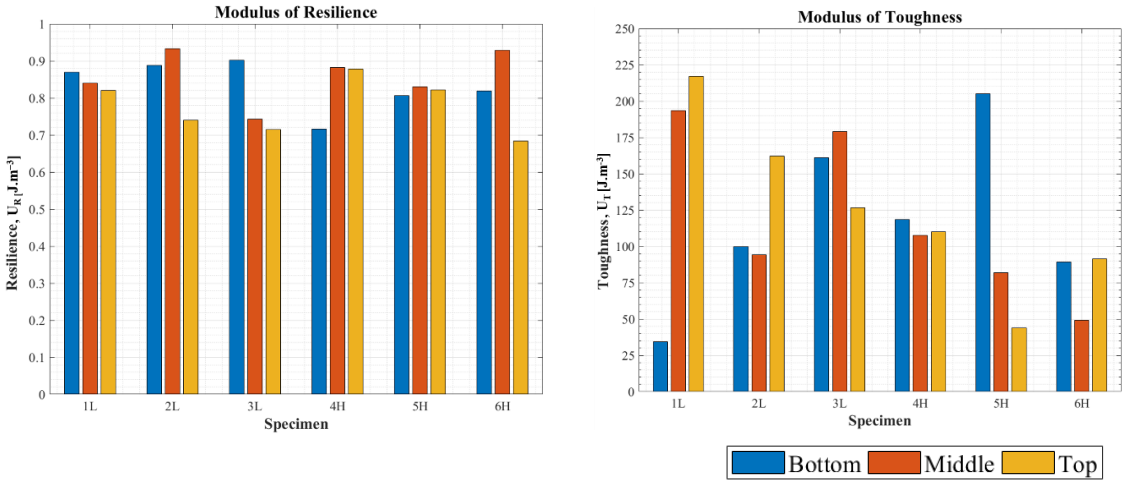

Figure 4.20 – Modulus of Resilience and Toughness.

From Figure 4.20, no visible pattern is possible to observe among the tested specimens regarding resilience or toughness. As previously noted, the expected result should indicate greater toughness in the middle region due to ductility increase. However, the

results may be considered as non-conclusive given the presence of subsurface defects, as pores, or manufacturing conditions.

Alongside this investigation, machining research on the same material was under development at DEMI-FCT-NOVA. The information collected complement the results reported so far and thus supports what is mentioning in this document. In this way, orthogonal machining of low heat-input revealed a pronounced decrease in specific cutting energy in the middle section. Additionally, milling operations on high heat-input samples revealed higher tool wear in the middle section as well. Although, both processes are physically different and assess different aspects of machining technology, the results were in agreement. The higher specific cutting energy and tool wear are associated with different material behaviour, more specifically, to the increased ductility in that region as was already explained and confirmed by the microhardness profiles. Tensile tests, however, did not confirm these suggestions, except for sample 3L. One reason may be the different aspects inherent to these processes. Tensile tests are substantially influenced by microcracks and other defects. And additionally, residual stresses were not under equal conditions since specimens for tensile testing and samples for machining were subjected to different preparation stages. Samples for machining studies were rectified but not cut.

Finally, Table 4.3 sums up the information derived from the uniaxial tensile tests and some observations on specimens subjected to SEM analysis and tests using VIC.

Table 4.3 – Uniaxial tensile testing results. Specimen "a" represents bottom, "b" middle and "c" top section.

Specimen	$\sigma_{0.2}$ [MPa]	UTS [MPa]	U_r [J.m^{-3}]	U_T [J.m^{-3}]	Observations
1La	596.6	819.6	0.87	34.48	Surface defect + incomplete fracture
1Lb	571.4	903.4	0.84	193.45	No visible defects
1Lc	572.8	913.9	0.82	217.20	No visible defects
2La	601.3	936.9	0.89	99.69	-
2Lb	615.6	884.7	0.93	94.25	-
2Lc	544.5	919.2	0.74	162.1	-
3La	610.5	935.4	0.90	161.01	No visible defects
3Lb	549.7	877.5	0.74	179.03	-
3Lc	537.6	898.2	0.72	126.60	-
4Ha	588.5	947.4	0.72	118.32	Surface defect
4Hb	610.0	857.7	0.88	107.51	Surface defect
4Hc	612.3	938.7	0.87	110.13	Surface defect
5Ha	576.4	929.5	0.81	205.00	-
5Hb	585.4	943.1	0.83	81.94	-
5Hc	574.3	921.6	0.82	43.68	Internal defect
6Ha	585.4	944.8	0.82	89.38	-
6Hb	616.6	866.7	0.93	49.00	-
6Hc	530.5	861.7	0.68	91.50	-

4.7 Fatigue testing results

The inspection performed by dye penetrant on all fatigue specimens prior testing did not reveal any superficial defects as pores or cracks, that would otherwise generate stress concentration and lead to premature crack initiation.

The first specimen subjected to testing was 7La and it reached the run-out limit set to 2×10^6 cycles. Consequently, for the next fatigue test specimen, 8Lb, the stress range was increased from 405 MPa to 450 MPa. However, the specimen reached the same number of cycles as the previous one without failure. Stress range was then increased to 495 MPa

and the number of cycles decreased to 155881. The subsequent testing parameters were established based on a compromise between maximum stress, σ_{max}, and expected number of cycles, N_f. Testing order, parameters and results are presented in Table 4.4, where N_f represents the number of cycles that each specimen endured until fracture.

Regression analysis was used to determine the mean and design curves of the experimental data. The mean S-N curve was obtained using equation (4.4) assuming N_f as the dependent variable. The correlation line fitted by equation (4.4) represents the average regression curve with 50% of probability of failure. The regression line is expressed by equation (4.5) in logarithmic notation, where *S* represents the stress range, N_f is the number of cycles to fracture, *C* is the fatigue strength coefficient and *m* is the fatigue strength exponent or the slope of the S-N curve. *C* and *m* are empirical constants, calculated from the experimental data. The results for *C* and *m* were 5.76×10^{14} and 3.62, respectively. The S-N curve, as a relation of stress range, $\Delta\sigma$, and number of cycles, N_f, is plotted in a log-log scale in Figure 4.21.

$$S^m \cdot N_f = C \tag{4.4}$$

$$log(N_f) = log(C) - m \cdot log\,(S) \tag{4.5}$$

In the same bi-logarithmic plot, data points represented by an arrow indicate run-out results. Additionally, the normal distribution is represented, symmetrical to the mean curve and is quantified by the standard deviation (SD), according to BS 7608:2014. Future fatigue data points are predicted to occur in-between the design curves, also known as confidence limit. According to the aforementioned standard, there is a failure probability of 2.3% below the design curve (mean curve – 2SD). The SD of the data was 0.127. Fatigue strength at 10^6 cycles, calculated according to the mean curve, was 263 MPa.

Table 4.4 – Fatigue test parameters and results.

Test order	Fatigue Specimen	Δσ [MPa]	σ_m [MPa]	σ_a [MPa]	Frequency [Hz]	N_f	Observations
1	7La	405	450	202.5	15	2000000	Run-out
5	7Lb	495	550	247.5	12	92771	
7	7Lc	472.5	525	236.25	12	97851	
4	8La	495	550	247.5	12	73300	
2	8Lb	450	500	225	12	2000000	Run-out
8	8Lc	472.5	525	236.25	12	112126	
9	9La	459	510	229.5	12	2000000	Run-out
6	9Lb	472.5	525	236.25	12	160099	
3	9Lc	495	550	247.5	12	155881	

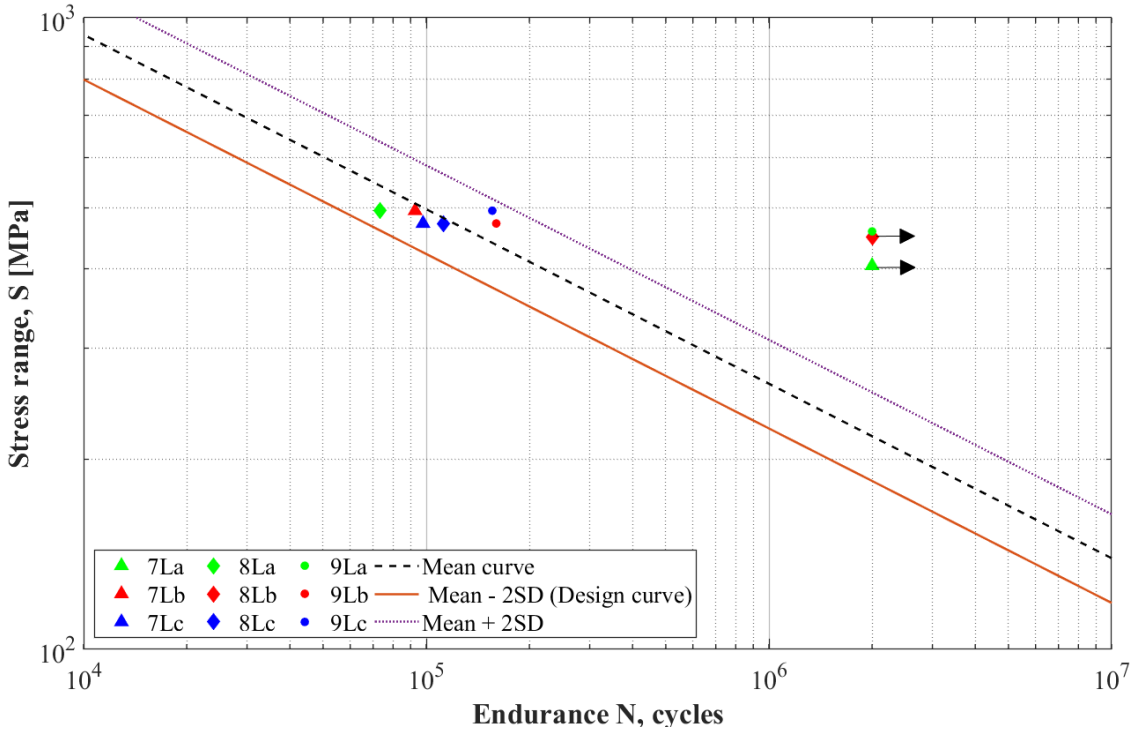

Figure 4.21 – S-N fatigue curve

Except for the three specimens that reached two million cycles without failure, the other six fractured within a range between 10^4 and 10^5 cycles. This feature suggests that fatigue testing was very close to low cycle fatigue (LCF) regime. Additionally, strain was observed to be mainly plastic, which is supported by the great ductility of the specimens observed during testing. As such, these observations lead to conclude that

strain-controlled instead of load-controlled testing would have been more appropriate and should be adopted in future investigations [60]. In case of strain-controlled testing, stress is an independent variable, and consequently it is easier to assess whether the material suffered dynamic hardening or softening.

The clip-gauge extensometer placed on specimen 9La allowed to assess the strain behaviour during testing. Figure 4.22 illustrates the results, where is possible to observe that minimum and maximum stress remained constant with respect to the number of cycles. However, mean strain continuously increased until near one thousand cycles, from which then remained constant until it reached 2×10^6 cycles. Among the many typical cyclic behaviours (Appendix A4), cyclic creep was observed to occur in this particular case, which is associated to forced-controlled conditions with unequal force limits ($R\neq-1$). This phenomenon is related to the continuous increase of the mean strain while strain amplitude remains constant [60, 61]. In this case, it is difficult to draw a conclusion, since although minimum and maximum strain increased in equal extent before it remained constant (around 1000 cycles), maximum stress was not high enough to produce fracture. This phenomenon, however, still lacks investigation as far as WAAM is concerned, and as such, should be considered in future studies.

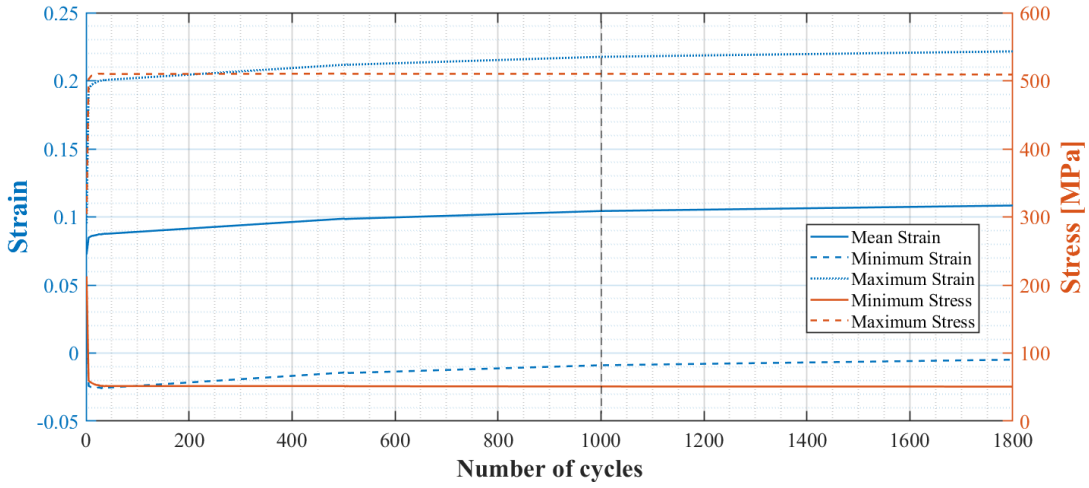

Figure 4.22 – Stress and strain progression with the number of cycles.

Fatigue is a very complex phenomenon that depends on many variables, not only testing parameters but also process conditions, specimens' preparation, surface roughness, microstructure, residual stresses, among others. Microstructure and residual stresses,

especially, play a key role in fatigue results. In this study, microstructure did not reveal significant differences between the three regions that were continuously described in this document. Grain size increased only slightly; grain distribution remained uniform throughout the vertical direction. Residual stresses, in turn, even if not analysed in this document, certainly affected tensile and fatigue tests. In other words, accumulated residual stresses, where released during specimens manufactured by EDM. The stress relaxation effect greatly influence mechanical properties, as was already mentioned in the literature review. The aspects described above may explain the results obtained from fatigue testing, since no conclusive difference was possible to observe along the wall's height.

4.7.1 Fractography

Ductile fracture involves large plastic deformation and are characterized by the presence of voids as a result of accommodating hard inclusions that do not deform at the same rate as the matrix. The finer and larger the number of inclusions in the material, higher is the probability of it to adopt a brittle behaviour, as Figure 4.23 exemplifies [63].

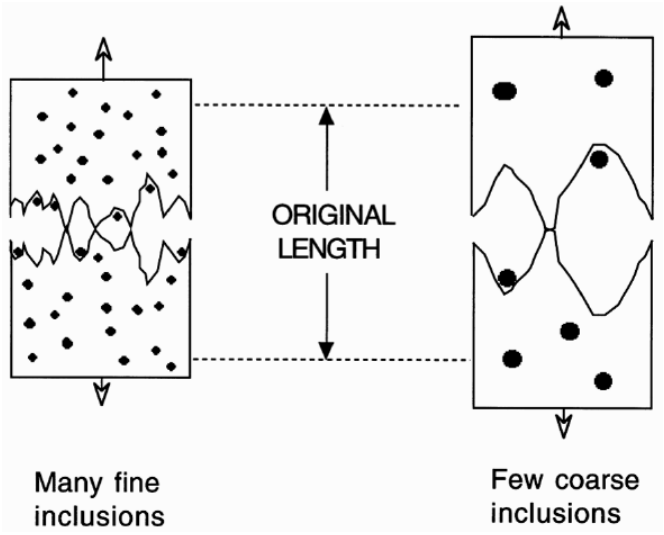

Figure 4.23 – Brittle vs ductile behaviour [63].

Fatigue fracture surfaces analysed in SEM revealed crack initiation near the edge, which suggests the absence of internal defects, as pores or entrapped inclusions. Additionally, micrographs analysis presented a ductile behaviour on all tested specimens.

Fatigue fractures occurred at stress levels below the YTS of the material. Fractures can initiate due to inclusions, external defects, grain boundary dislocations or geometric discontinuities. From fracture surfaces analysis, two types of surface crack initiation were observed. Corner quarter-elliptical cracks as a result of geometry discontinuity and semi-elliptical cracks, the first represented in Figure 4.24 and the latter in Figure 4.25, with respective micrographs of subsequent fracture surface observations. Mixed mechanisms of crack propagation occurred. Fibrous fracture initially represented by fatigue striations, where each striation spacing describes the crack progression in each cycle. Crack propagation, in this case, occurred perpendicularly to the maximum stress direction as represented by the arrow illustrated in micrographs 2 and 4 of Figure 4.25. Towards the end, the surface presents an irregular aspect which corresponds to a ductile fracture, with the presence of voids, or also known as dimples, as displayed in micrograph 4 of Figure 4.24, each accommodating a spherical shape inclusion, that through EDS analysis it revealed a higher Mn content, Figure 4.26. Similar fracture surface observations were made in Refs [56, 59]. Additionally, among the different regions (bottom, middle and top), no difference was observed regarding crack nucleation and propagation, which suggests that sample's height does not have significant influence on the fatigue behaviour of the produced parts. However, this characteristic demands further and more detailed investigation.

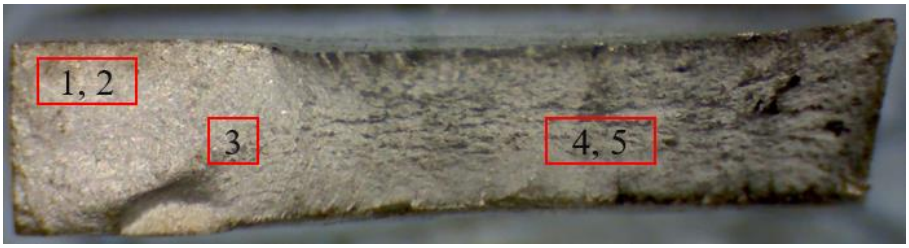

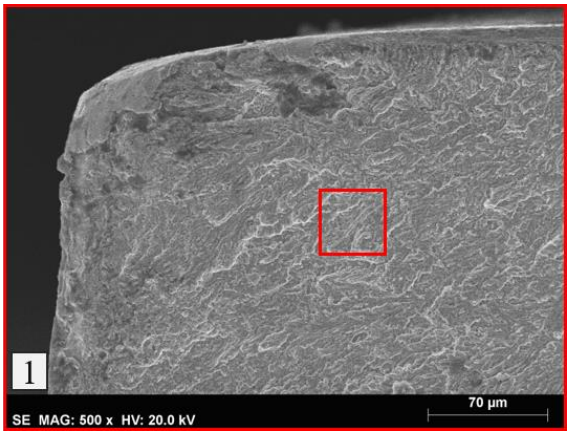

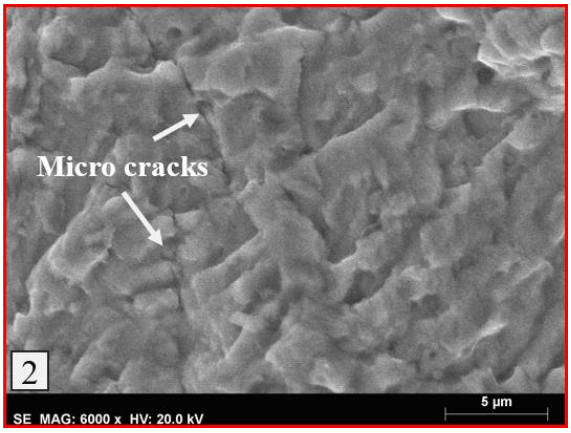

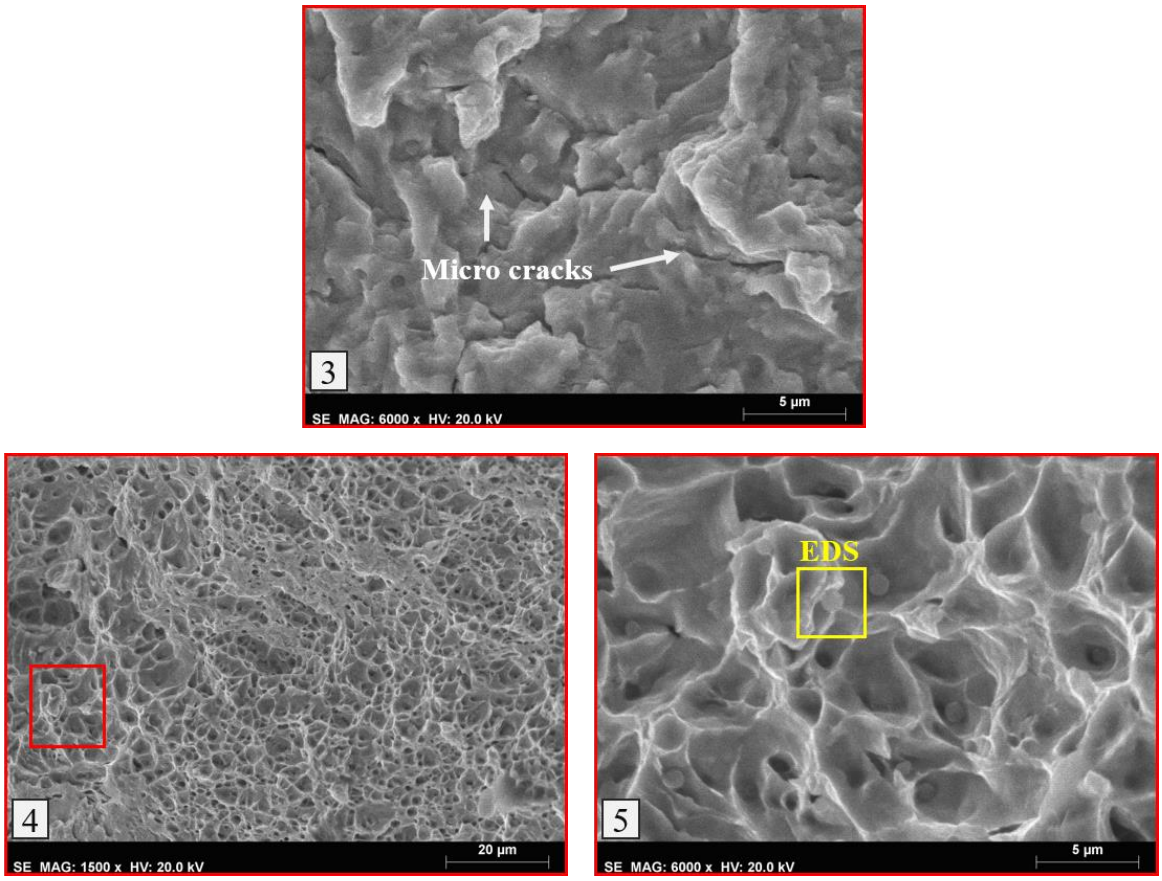

Figure 4.24 – Sequence of fracture surface images of 10Lb specimen: 1. Crack nucleation, 2. Fatigue Striations, 3. Fracture propagation and 4 and 5. Ductile fracture (dimples and inclusions).

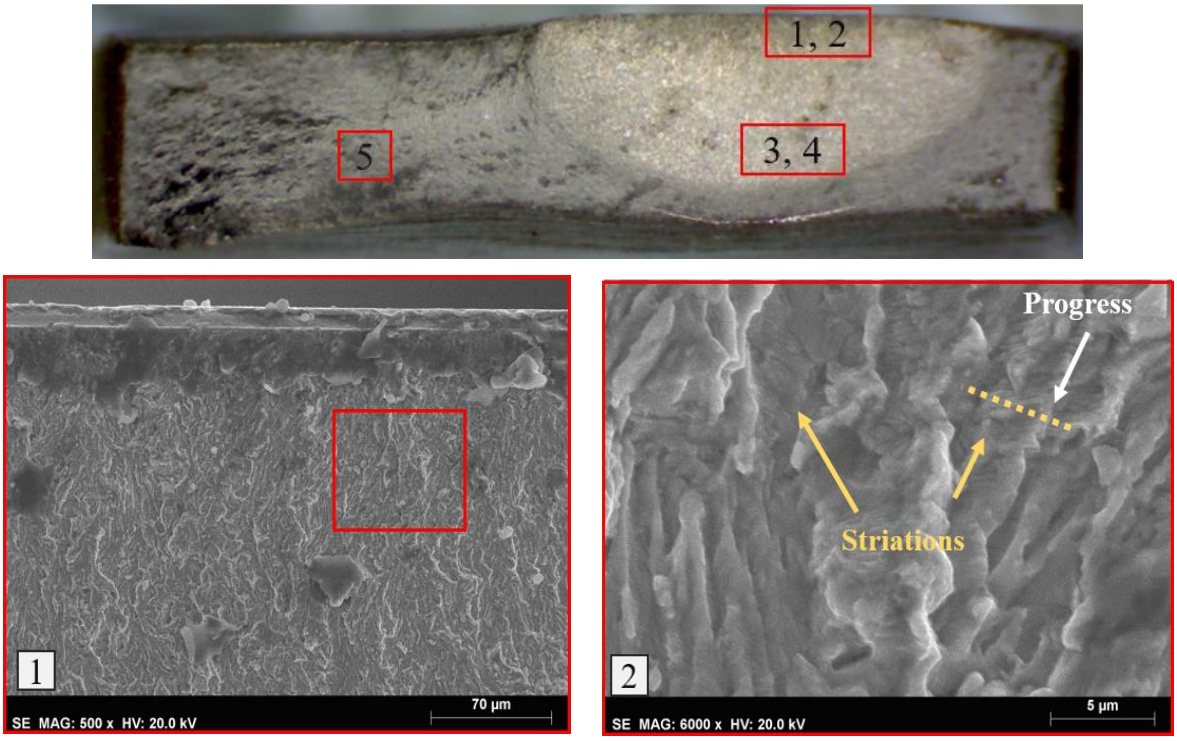

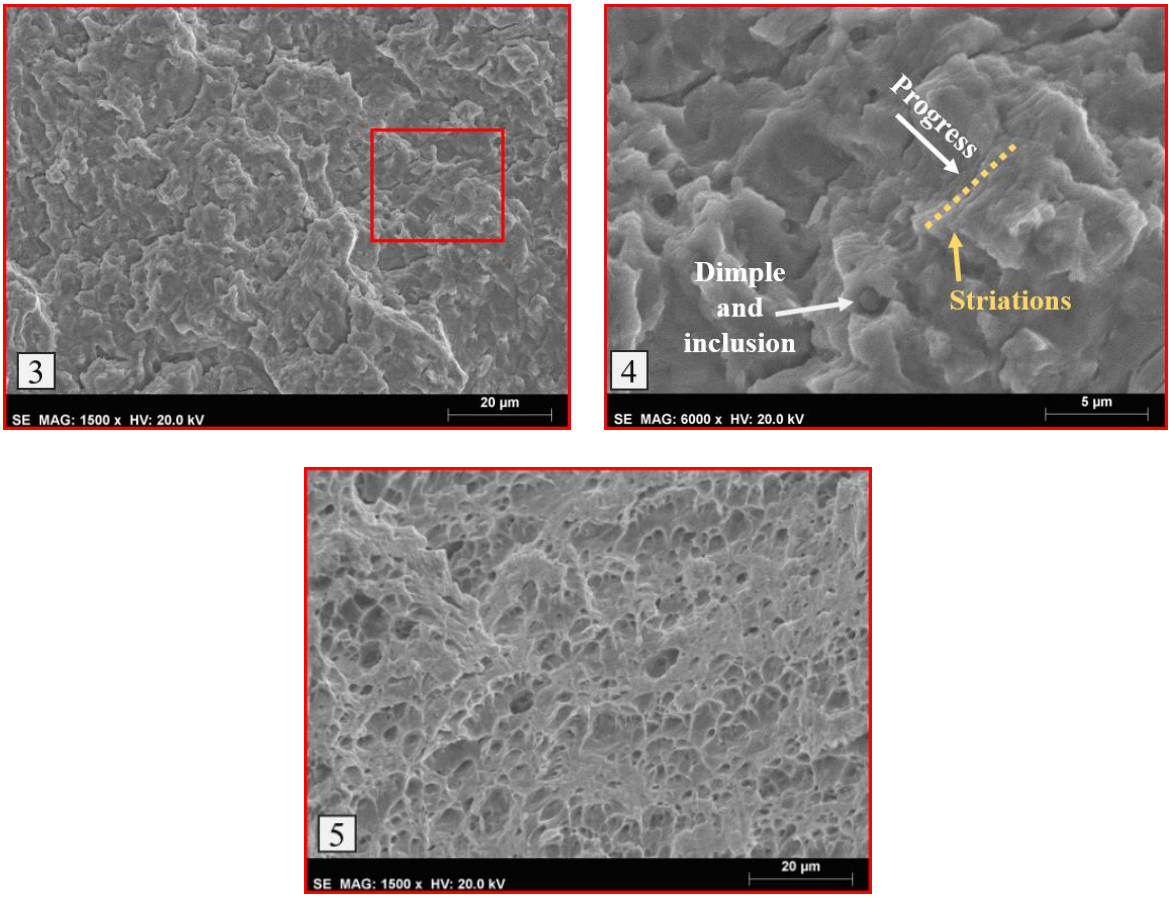

Figure 4.25 – Sequence of fracture surface images of 10Lc specimen: 1. Crack initiation, 2. Fatigue striations, 3. Crack propagation – secondary fracture, 4. Fatigue striations and 5. Unstable fatigue crack.

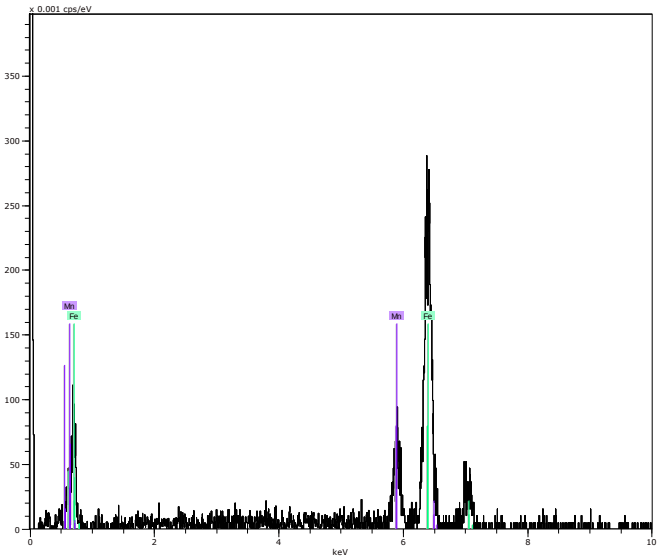

Figure 4.26 – EDS spectrum of particle inclusion.

Finally, after SEM analysis of the fatigue fracture surfaces fracture, EDS analysis was performed in order to assess part's chemical composition in comparison with the material datasheet. The result, displayed in Figure 4.27, showed similar composition, which was in compliance with the data provided by the wire manufacturer.

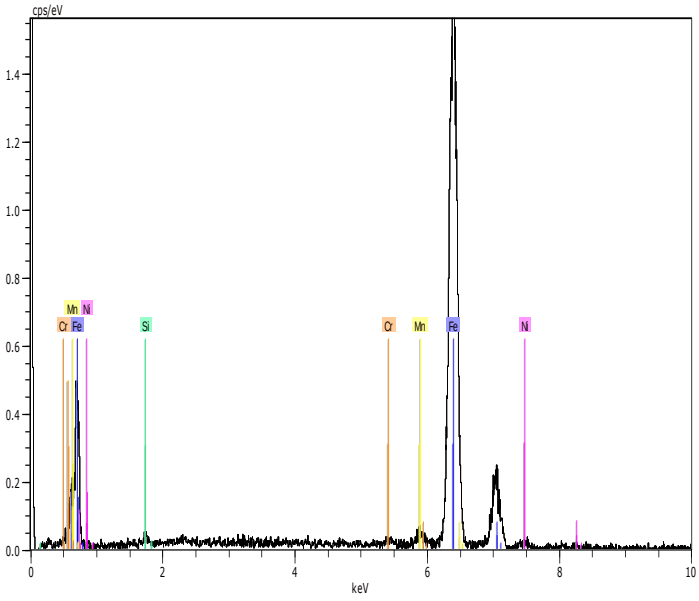

Figure 4.27 – EDS analysis on HSLA specimen.

4.8 Chapter resume

This chapter presents all the results obtained from the experimental work and intends to give them a comprehensive explanation, relating, at each step, the manufacturing process with the many phenomena observed.

All samples were analysed first from a macroscopic perspective, i.e., visual inspection and waviness measurements, followed by NDT techniques such as electrical conductivity and eddy currents testing and were finally complemented by microhardness measurements along samples height. Tensile and fatigue tests were performed, and all results were analysed, establishing the main differences concerning heat input and specimens' location upon the wall. Finally, fractography observations were presented, together with a detailed analysis.

The next chapter summarizes the main conclusions derived from this investigation and the contributions made towards the progress of WAAM technology. Additionally, suggestions of future work are proposed.

5 Conclusions and Future Work

5.1 Conclusions

The quest for improved mechanical properties, weldability, reduced costs, and post-processing makes the advent of WAAM a driving force technology in today's industry. In turn, HSLA steels are gaining widespread use in industries such as automotive, offshore structure or shipbuilding, and hence, its combination with WAAM is prone to directly compete with conventional technologies. However, as it was already reported in this document, WAAM still needs vast research in order to improve and be implemented in the industry, especially as far as mechanical properties are concerned.

This thesis aimed to contribute to the development of this technology by manufacturing parts with two different heat inputs and subsequently applying characterization techniques in order to better understand the influence that heat input and height has on mechanical properties.

In a first stage, thin-walled parts were manufactured on a custom-built welding torch mounted on a three-axis positioning system. Following, all parts were processed in order to obtain samples for microscopic analysis, microhardness measurements, NDT inspection, and mechanical tests, especially, tensile and fatigue tests.

Based on the analysis of this research, the following conclusions can be drawn:

- An important conclusion of this work is that process conditions have a determinant effect on mechanical properties. In other words, in case of longer stops, longer than the predefined dwell time, parts experience different thermal

cycles and consequently there are changes in microstructure, microhardness and properties such as ductility and/or toughness.

- Electrical conductivity as well as magnetic permeability were uniform along height, despite the heat accumulation. Moreover, low heat-input parts presented a slight electrical resistance increase, relative to high heat-input, which can be associated to the increased number of grain boundaries that restrict the electrical flow.
- Microscopic analysis did not reveal the existence of pores or inclusions.
- Grain size was observed to slightly increase on high heat-input parts.
- Along height, courser grain was observed in the middle region compared with bottom and top regions.
- Microstructure was observed to be of pearlite and mainly acicular ferrite, which particularly offers increased material toughness and strength.
- An 15% decrease in microhardness was observed from low to high heat-input.
- In normal processing conditions, i.e., exempt of any stops, microhardness decreased towards the middle and increased in the last layers, Thus, the material adopted a pronounced ductile behaviour in the middle region.
- Yield strength (YTS) decreased 35% on average compared to the wire material datasheet.
- No visible pattern was observed between the different heat input parts, as well as different parts regions, as far as mechanical properties such as resilience, toughness and YTS are concerned. A very plausible reason can be the presence of subsurface defects, that invalidate the results. In addition, under normal processing conditions, there is a small decrease of UTS in the middle regions.
- Fatigue results were consistent along height.
- Fatigue strength at 10^6 cycles, calculated according to the mean curve, was 263 MPa.
- The strain monitoring during fatigue testing revealed cyclic creep behaviour, i.e., continuous mean strain increase despite stress remaining constant.
- SEM observations of fatigue fracture surfaces confirmed the ductile behaviour inherent of this material. Fatigue striations and dimples were observed.
- Two types of surface crack initiation were observed resulting in two crack geometries: corner quarter-elliptical and semi-elliptical cracks.

- EDS analysis revealed similar chemical composition compared to the material data sheet.
- Overall, low heat-input parts yielded improved mechanical properties due to shorter thermal cycles that lead to a smaller grain size and a harder microstructure. In addition, these parts provide higher productivity given the faster travel speed during manufacturing.
- Although there is no height limit beyond the one established by the manufacturing machine, it is clear that the middle region will always experience greater heat accumulation, which will affect properties as ductility or tensile strength.
- The aspect mentioned above will significantly affect milling performance, depending on the region that is being processed. Low heat-input, as already referred in previous studies, has better results than high heat-input parts, which may be explained by the increased ductility and coarser grain the latter presented.

5.2 Future work

It is clear that further research should be conducted on this subject to better comprehend how mechanical properties are influenced by the process conditions and parts geometry. Hence, some suggestions are presented for future investigations:

- Assessment of residual stresses and their influence on mechanical properties studied in this work.
- Perform strain-controlled fatigue tests under LCF regime and compare with the results obtained in this work.
- Tensile and fatigue assessment of crosswise and lengthwise specimens.
- Different dwell time between high heat-input and low heat-input parts in order to start deposition at the same temperature.
- Numerical simulation in order to assess heat dissipation and residual stresses.
- Investigate the possibility of multipass welding and respective mechanical properties when thicker parts are required.
- Mechanical properties assessment of more complex part geometry.

Bibliography

[1] M. Di Nicolantonio, Advances in Intelligent Systems and Computing 975 Advances in Additive Manufacturing , Modeling Systems and 3D Prototyping, 2019.

[2] P. Zawadzki, K. Zywicki, Smart product design and production control for effective mass customization in the industry 4.0 concept, Manag. Prod. Eng. Rev. 7 (2016) 105–112. https://doi.org/10.1515/mper-2016-0030.

[3] Z. Zeng, B.. Cong, J.P. Oliveira, W.. Ke, N. Schell, B. Peng, Z.W. Qi, F.. Ge, W. Zhang, S.S. Ao, Wire and arc additive manufacturing of a Ni-rich NiTi shape memory alloy: microstructure and mechanical properties, Addit. Manuf. (2020) 101051. https://doi.org/10.1016/j.addma.2020.101051.

[4] B. Dutta, S. Babu, B. Jared, Metal additive manufacturing, in: Sci. Technol. Appl. Met. Addit. Manuf., Elsevier, 2019: pp. 1–10. https://doi.org/10.1016/B978-0-12-816634-5.00001-7.

[5] U.M. Dilberoglu, B. Gharehpapagh, U. Yaman, M. Dolen, The Role of Additive Manufacturing in the Era of Industry 4.0, Procedia Manuf. (2017). https://doi.org/10.1016/j.promfg.2017.07.148.

[6] ASTM International, F2792-12a - Standard Terminology for Additive Manufacturing Technologies, Rapid Manuf. Assoc. (2013) 10–12. https://doi.org/10.1520/F2792-12A.2.

[7] P. Kattire, A review on powder bed fusion technology of metal additive manufacturing, 2014.

[8] T.A. Rodrigues, V. Duarte, R.M. Miranda, T.G. Santos, J.P. Oliveira, Current status and perspectives on wire and arc additive manufacturing (WAAM), Materials (Basel). 12 (2019). https://doi.org/10.3390/ma12071121.

[9] J.J. Lewandowski, M. Seifi, Metal Additive Manufacturing: A Review of Mechanical Properties, Annu. Rev. Mater. Res. 46 (2016) 151–186. https://doi.org/10.1146/annurev-matsci-070115-032024.

[10] C. V. Haden, G. Zeng, F.M. Carter, C. Ruhl, B.A. Krick, D.G. Harlow, Wire and

arc additive manufactured steel: Tensile and wear properties, Addit. Manuf. 16 (2017) 115–123. https://doi.org/10.1016/j.addma.2017.05.010.

[11] S.W. Williams, F. Martina, A.C. Addison, J. Ding, G. Pardal, P. Colegrove, Wire + Arc additive manufacturing, Mater. Sci. Technol. (United Kingdom). 32 (2016) 641–647. https://doi.org/10.1179/1743284715Y.0000000073.

[12] T. DebRoy, H.L. Wei, J.S. Zuback, T. Mukherjee, J.W. Elmer, J.O. Milewski, A.M. Beese, A. Wilson-Heid, A. De, W. Zhang, Additive manufacturing of metallic components – Process, structure and properties, Prog. Mater. Sci. 92 (2018) 112–224. https://doi.org/10.1016/j.pmatsci.2017.10.001.

[13] J.P. Oliveira, T.G. Santos, R.M. Miranda, Revisiting fundamental welding concepts to improve additive manufacturing: From theory to practice, Prog. Mater. Sci. (2019) 100590. https://doi.org/10.1016/j.pmatsci.2019.100590.

[14] D. Ding, Z. Pan, D. Cuiuri, H. Li, Wire-feed additive manufacturing of metal components: technologies, developments and future interests, Int. J. Adv. Manuf. Technol. 81 (2015) 465–481. https://doi.org/10.1007/s00170-015-7077-3.

[15] R. Baker, METHOD OF MAKING DECORATIVE ARTICLES, 1925.

[16] D.H. Phillips, Welding Engineering, 2016.

[17] E.M. Ryan, On Wire and Arc Additive Manufacture of Aluminium, 2018.

[18] B. Wu, Z. Pan, D. Ding, D. Cuiuri, H. Li, J. Xu, J. Norrish, A review of the wire arc additive manufacturing of metals: properties, defects and quality improvement, J. Manuf. Process. 35 (2018) 127–139. https://doi.org/10.1016/j.jmapro.2018.08.001.

[19] Ivántabernero, A. Paskual, P. Álvarez, A. Suárez, Study on Arc Welding Processes for High Deposition Rate Additive Manufacturing, in: Procedia CIRP, Elsevier B.V., 2018: pp. 358–362. https://doi.org/10.1016/j.procir.2017.12.095.

[20] J. Lopes, Feasibility of the milling process on HSLA parts manufactured with Wire and arc additive manufacturing, 2019.

[21] W.D. Callister, Material Science and Engineering, 2007.

[22] C.M. Branco, Mecânica dos Materiais, 5th ed., Fundação Calouste Gulbenkian, 1994.

[23] N.E. Dowling, Mechanical Behaviou of materials: Engineering methods for deformations, fracture and fatigue, 4th ed., 2012.

[24] ASTM E8 / E8M-16a, Standard test methods for tension testing of metallic materials, (2016). https://doi.org/10.1520/E0008.

[25] ASTM E1823 - 13, Standard Terminology Relating to Fatigue and Fracture Testing, (2013). https://doi.org/10.1520/E1823-13.

[26] J. Schijve, Fatigue of Structures and Materials, 2nd ed., Springer, Dordrecht, Delft, The Netherlands, 2009. https://doi.org/https://doi.org/10.1007/978-1-4020-6808-9.

[27] R.L. Smith, Fatigue of metals, J. Franklin Inst. 256 (1953) 588–589. https://doi.org/10.1016/0016-0032(53)91169-7.

[28] A. Carpinteri, Fatigue crack, Weld. Cut. 12 (2013) 299.

[29] J. V. Gordon, C. V. Haden, H.F. Nied, R.P. Vinci, D.G. Harlow, Fatigue crack growth anisotropy, texture and residual stress in austenitic steel made by wire and arc additive manufacturing, Mater. Sci. Eng. A. 724 (2018) 431–438. https://doi.org/10.1016/j.msea.2018.03.075.

[30] P.A. Colegrove, J. Donoghue, F. Martina, J. Gu, P. Prangnell, J. Hönnige, Application of bulk deformation methods for microstructural and material property improvement and residual stress and distortion control in additively manufactured components, Scr. Mater. 135 (2017) 111–118. https://doi.org/10.1016/j.scriptamat.2016.10.031.

[31] ASTM, E 466 – 96 - Standard Practice for Conducting Force Controlled Constant Amplitude Axial Fatigue Tests of Metallic Materials., Astm Int. (2002). https://doi.org/10.1520/E0466-07.2.

[32] S. Suryakumar, K.P. Karunakaran, A study of the mechanical properties of objects built through weld- deposition, 227 (2013) 1138–1147. https://doi.org/10.1177/0954405413482122.

[33] A. Ermakova, A. Mehmanparast, S. Ganguly, A review of present status and challenges of using additive manufacturing technology for offshore wind applications, Procedia Struct. Integr. 17 (2019) 29–36. https://doi.org/10.1016/j.prostr.2019.08.005.

[34] E.A. Alberti, B.M.P. Bueno, A.S.C.M. D'Oliveira, Additive manufacturing using plasma transferred arc, Int. J. Adv. Manuf. Technol. 83 (2016) 1861–1871. https://doi.org/10.1007/s00170-015-7697-7.

[35] W. Liu, F. Lu, Y. Wei, Y. Ding, P. Wang, X. Tang, Special zone in multi-layer and multi-pass welded metal and its role in the creep behavior of 9Cr1Mo welded joint, Mater. Des. 108 (2016) 195–206. https://doi.org/10.1016/j.matdes.2016.06.102.

[36] S. Ragu Nathan, V. Balasubramanian, S. Malarvizhi, A.G. Rao, Effect of welding processes on mechanical and microstructural characteristics of high strength low alloy naval grade steel joints, Def. Technol. 11 (2015) 308–317. https://doi.org/10.1016/j.dt.2015.06.001.

[37] Y. Shao, C. Liu, Z. Yan, H. Li, Y. Liu, Journal of Materials Science & Technology Formation mechanism and control methods of acicular ferrite in HSLA steels : A review, J. Mater. Sci. Technol. 34 (2018) 737–744. https://doi.org/10.1016/j.jmst.2017.11.020.

[38] D.A. Skobir, HIGH-STRENGTH LOW-ALLOY (HSLA) STEELS VISOKOTRDNA MALOLEGIRANA (HSLA) KONSTRUKCIJSKA JEKLA, n.d.

[39] T.A. Rodrigues, V. Duarte, J.A. Avila, T.G. Santos, R.M. Miranda, J.P. Oliveira, Wire and arc additive manufacturing of HSLA steel: Effect of thermal cycles on microstructure and mechanical properties, Addit. Manuf. 27 (2019) 440–450. https://doi.org/10.1016/j.addma.2019.03.029.

[40] S. Bandgar, C. Gupta, G. Rao, P. Malik, R.N. Singh, K. Sridhar, Fatigue Crack Growth Rate Behaviour of HSLA Steel at Varying Load Amplitudes, Procedia Struct. Integr. 14 (2019) 330–336. https://doi.org/10.1016/j.prostr.2019.05.041.

[41] J. Zhang, X. Wang, S. Paddea, X. Zhang, Fatigue crack propagation behaviour in wire+arc additive manufactured Ti-6Al-4V: Effects of microstructure and residual stress, Mater. Des. 90 (2016) 551–561. https://doi.org/10.1016/j.matdes.2015.10.141.

[42] J. Gordon, J. Hochhalter, C. Haden, D.G. Harlow, Enhancement in fatigue performance of metastable austenitic stainless steel through directed energy deposition additive manufacturing, Mater. Des. (2019).

https://doi.org/10.1016/j.matdes.2019.107630.

[43] R. Biswal, X. Zhang, A.K. Syed, M. Awd, J. Ding, F. Walther, S. Williams, Criticality of porosity defects on the fatigue performance of wire + arc additive manufactured titanium alloy, Int. J. Fatigue. 122 (2019) 208–217. https://doi.org/10.1016/j.ijfatigue.2019.01.017.

[44] R. Biswal, X. Zhang, M. Shamir, A. Al Mamun, M. Awd, F. Walther, A. Khadar Syed, Interrupted fatigue testing with periodic tomography to monitor porosity defects in wire + arc additive manufactured Ti-6Al-4V, Addit. Manuf. 28 (2019) 517–527. https://doi.org/10.1016/j.addma.2019.04.026.

[45] T.R. Smith, J.D. Sugar, J.M. Schoenung, C. San Marchi, Relationship between manufacturing defects and fatigue properties of additive manufactured austenitic stainless steel, Mater. Sci. Eng. A. 765 (2019) 138268. https://doi.org/10.1016/j.msea.2019.138268.

[46] X. Zhang, F. Martina, J. Ding, X. Wang, S.W. Williams, Fracture toughness and fatigue crack growth rate properties in wire + arc additive manufactured Ti-6Al-4V, Fatigue Fract. Eng. Mater. Struct. 40 (2017) 790–803. https://doi.org/10.1111/ffe.12547.

[47] M. Wächter, M. Leicher, M. Hupka, C. Leistner, L. Masendorf, K. Treutler, S. Kamper, A. Esderts, V. Wesling, S. Hartmann, Monotonic and fatigue properties of steel material manufactured by wire arc additive manufacturing, Appl. Sci. 10 (2020). https://doi.org/10.3390/APP10155238.

[48] T. Ron, G.K. Levy, O. Dolev, A. Leon, A. Shirizly, E. Aghion, The effect of microstructural imperfections on corrosion fatigue of additively manufactured ER70S-6 alloy produced by wire arc deposition, Metals (Basel). 10 (2020). https://doi.org/10.3390/met10010098.

[49] Dratec, DT-X90 MSG -Drahtelektrode, (2017) 16834.

[50] Gama Alphagaz | Air Liquide Healthcare Portugual, (n.d.). https://www.airliquidehealthcare.pt/gama-alphagaz (accessed November 26, 2020).

[51] H. Geng, J. Li, J. Xiong, X. Lin, D. Huang, F. Zhang, Formation and improvement of surface waviness for additive manufacturing 5A06 aluminium alloy component

with GTAW system, Rapid Prototyp. J. 24 (2018) 342–350. https://doi.org/10.1108/RPJ-04-2016-0064.

[52] A.N. AbdAlla, M.A. Faraj, F. Samsuri, D. Rifai, K. Ali, Y. Al-Douri, Challenges in improving the performance of eddy current testing: Review, Meas. Control (United Kingdom). 52 (2019) 46–64. https://doi.org/10.1177/0020294018801382.

[53] G.L. Sorger, J.P. Oliveira, P.L. Inácio, N. Enzinger, P. Vilaça, R.M. Miranda, T.G. Santos, Non-destructive microstructural analysis by electrical conductivity: Comparison with hardness measurements in different materials, J. Mater. Sci. Technol. 35 (2019) 360–368. https://doi.org/10.1016/j.jmst.2018.09.047.

[54] Four-Point Probe Manual, (n.d.). http://four-point-probes.com/four-point-probe-manual/ (accessed August 15, 2020).

[55] International Standard ISO, Metallic materials - Vickers hardness test - Part 1 : Test method (ISO 6507-1 : 2018), Int. Stand. (2018) 1–49. https://doi.org/ISO 6507-1 : 2018.

[56] V. Geantă, I. Voiculescu, R. Ștefănoiu, E.R. Rusu, Stainless steels with biocompatible properties for medical devices, Key Eng. Mater. 583 (2014) 9–15. https://doi.org/10.4028/www.scientific.net/KEM.583.9.

[57] P. Dirisu, S. Ganguly, A. Mehmanparast, F. Martina, S. Williams, Analysis of fracture toughness properties of wire + arc additive manufactured high strength low alloy structural steel components, Mater. Sci. Eng. A. 765 (2019) 138285. https://doi.org/10.1016/j.msea.2019.138285.

[58] International AWS, Effect of Chemical Elements in Steel, n.d.

[59] A. Ermakova, A. Mehmanparast, S. Ganguly, J. Razavi, F. Berto, Investigation of mechanical and fracture properties of wire and arc additively manufactured low carbon steel components, Theor. Appl. Fract. Mech. 109 (2020) 102685. https://doi.org/10.1016/j.tafmec.2020.102685.

[60] V. Aleksić, L. Milović, I. Blačić, T. Vuherer, S. Bulatović, Effect of LCF on behavior and microstructure of microalloyed HSLA steel and its simulated CGHAZ, Eng. Fail. Anal. 104 (2019) 1094–1106. https://doi.org/10.1016/j.engfailanal.2019.06.017.

[61] H.D. Chandler, S. Kwofie, A description of cyclic creep under conditions of axial

cyclic and mean stresses, Int. J. Fatigue. 27 (2005) 541–545. https://doi.org/10.1016/j.ijfatigue.2004.09.009.

[62] H.F.S.G. Ferreira, Comportamento à fadiga de componentes estruturais sob a acção de solicitações de amplitude variável, Faculdade de Engenharia da Universidade do Porto, 2006.

[63] A. Ermakova, A. Mehmanparast, S. Ganguly, A review of present status and challenges of using additive manufacturing technology for offshore wind applications, Procedia Struct. Integr. 17 (2019) 29–36. https://doi.org/10.1016/j.prostr.2019.08.005.

Appendix

A1 – Designed Specimens

Uniaxial tensile testing specimens **Fatigue testing specimens**

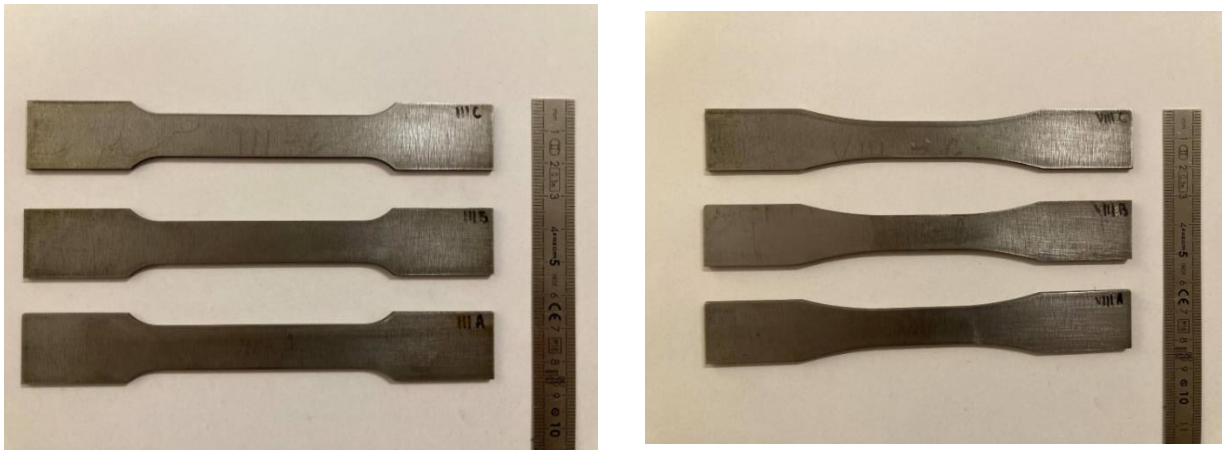

Figure A.1 – Tensile and fatigue specimens produced by EDM.

A2 – Microhardness measurements

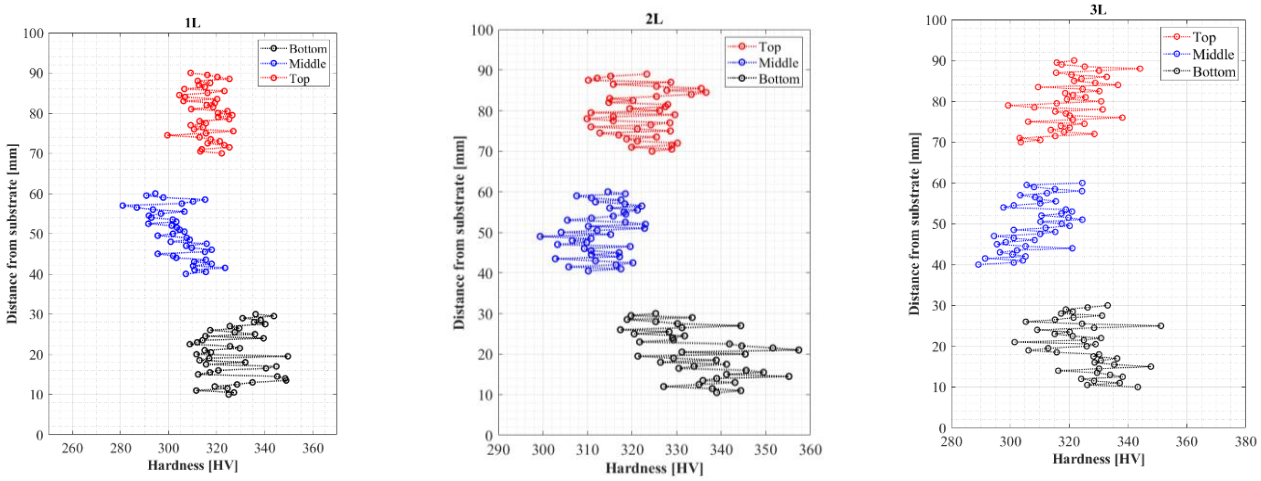

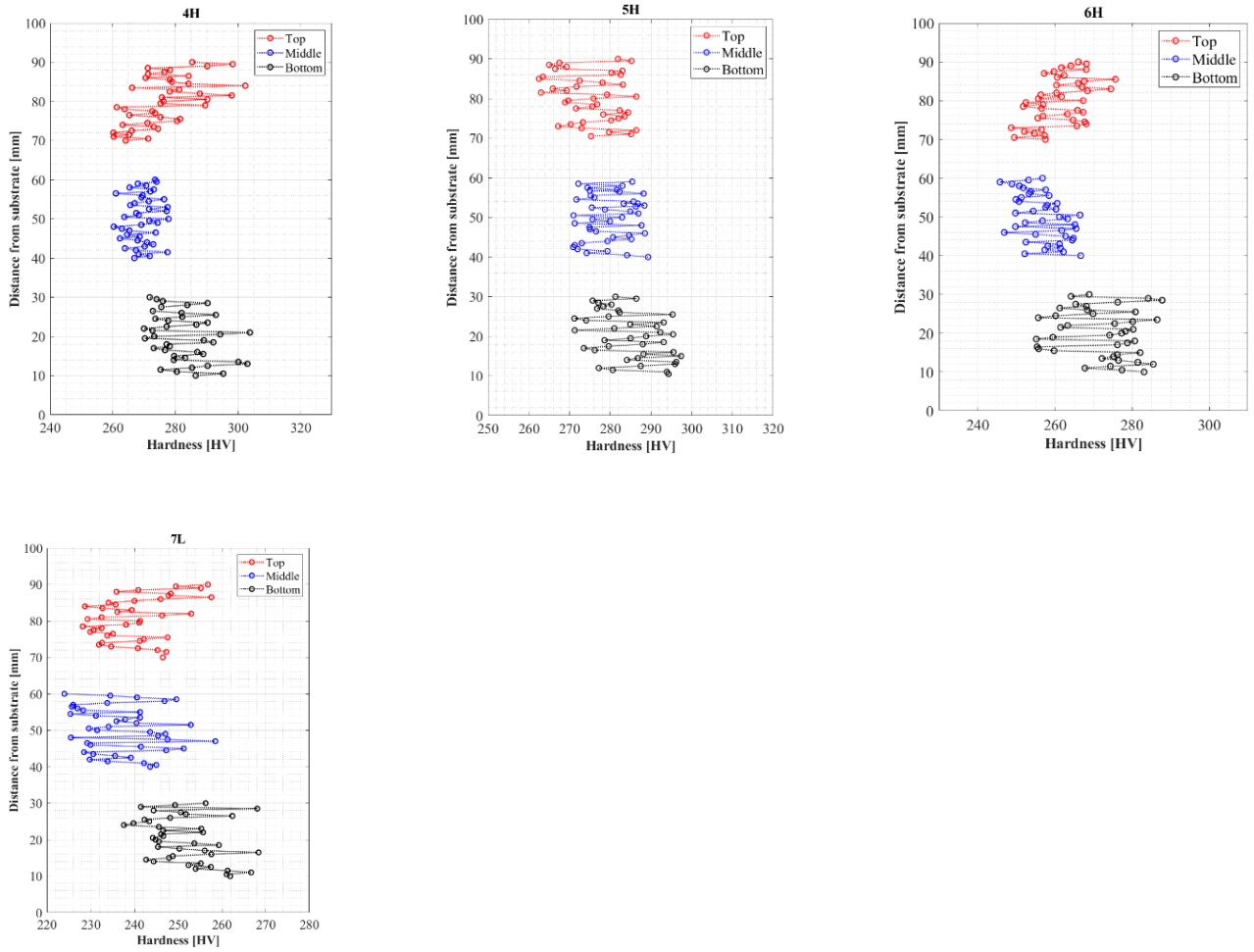

Figure A2.1 – Microhardness profiles.

A3 – Specimens surface roughness

Table A3.1 – Surface roughness measurements of fatigue and tensile specimens.

Sample	Position	Ra [µm]	Rz [µm]
1L	Bottom	1.33 ± 0.63	8.81 ± 3.88
	Middle	1.49 ±0.10	11.71 ± 0.97
	Top	1.38 ± 0.12	11.19 ± 0.51
2L	Bottom	1.50 ±0.32	10.63 ± 2.10
	Middle	1.35 ± 0.07	11.59 ± 0.66
	Top	1.41 ± 0.19	11.39 ± 1.00
3L	Bottom	1.46 ± 0.05	11.42 ± 0.46
	Middle	1.23 ± 0.23	9.93 ± 1.81
	Top	1.50 ± 0.16	11.29 ± 0.87
4H	Bottom	1.75 ± 0.15	10.49 ± 0.57
	Middle	1.79 ± 0.17	11.00 ± 0.99
	Top	1.56 ± 0.13	9.86 ± 0.64
5H	Bottom	1.67 ± 0.15	9.83 ± 0.57
	Middle	1.76 ± 0.19	10.82 ± 1.27
	Top	1.78 ± 0.18	9.54 ± 1.01
6H	Bottom	1.69 ± 0.19	10.36 ± 0.87
	Middle	1.34 ± 0.28	8.46 ± 1.53
	Top	1.72 ± 0.15	10.04 ± 0.68
7L	Bottom	1.13 ± 0.13	8.94 ± 1.03
	Middle	1.28 ± 0.16	9.41 ± 0.57
	Top	1.20 ± 0.12	10.22 ± 1.81
8L	Bottom	1.39 ± 0.06	11.00 ±0.53
	Middle	1.23 ± 0.19	10.39 ±2.24
	Top	1.16 ± 0.08	9.10 ±1.09
9L	Bottom	1.39 ± 0.12	10.33 ± 1.09
	Middle	1.48 ± 0.23	11.13 ± 1.02
	Top	1.14 ± 0.17	8.56 ± 1.52

A4 – Cyclic behaviour on fatigue tests

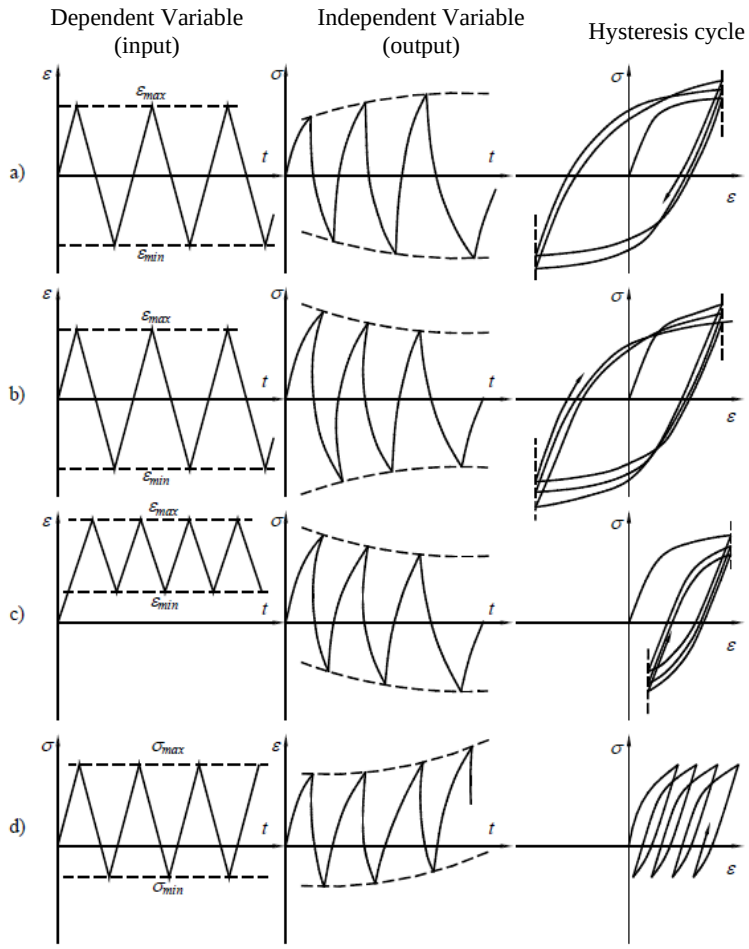

Figure A4.1 – Typical cyclic behaviour: a) cyclic hardening; b) cyclic softening; c) cyclic relaxation of the mean stress; d) Cyclic creep (adapted from [62]).